JACS
JOURNAL OF THE AMERICAN CHEMICAL SOCIETY
pubs.acs.org/JACS
Article

Controlling the Reactivity of a Metal-Hydroxo Adduct with a Hydrogen Bond

Adedamola A. Opalade, Logan Hessefort, Victor W. Day, and Timothy A. Jackson*

Cite This: *J. Am. Chem. Soc.* 2021, 143, 15159−15175

Read Online

ACCESS | Metrics & More | Article Recommendations | Supporting Information

ABSTRACT: The enzymes manganese lipoxygenase (MnLOX) and manganese superoxide dismutase (MnSOD) utilize mononuclear Mn centers to effect their catalytic reactions. In the oxidized Mn^{III} state, the active site of each enzyme contains a hydroxo ligand, and X-ray crystal structures imply a hydrogen bond between this hydroxo ligand and a *cis* carboxylate ligand. While hydrogen bonding is a common feature of enzyme active sites, the importance of this particular hydroxo-carboxylate interaction is relatively unexplored. In this present study, we examined a pair of Mn^{III}-hydroxo complexes that differ by a single functional group. One of these complexes, $[Mn^{III}(OH)(PaPy_2N)]^+$, contains a naphthyridinyl moiety capable of forming an intramolecular hydrogen bond with the hydroxo ligand. The second complex, $[Mn^{III}(OH)(PaPy_2Q)]^+$, contains a quinolinyl moiety that does not permit any intramolecular hydrogen bonding. Spectroscopic characterization of these complexes supports a common structure, but with perturbations to $[Mn^{III}(OH)(PaPy_2N)]^+$, consistent with a hydrogen bond. Kinetic studies using a variety of substrates with activated O−H bonds, revealed that $[Mn^{III}(OH)(PaPy_2N)]^+$ is far more reactive than $[Mn^{III}(OH)(PaPy_2Q)]^+$, with rate enhancements of 15−100-fold. A detailed analysis of the thermodynamic contributions to these reactions using DFT computations reveals that the former complex is significantly more basic. This increased basicity counteracts the more negative reduction potential of this complex, leading to a stronger O−H BDFE in the $[Mn^{II}(OH_2)(PaPy_2N)]^+$ product. Thus, the differences in reactivity between $[Mn^{III}(OH)(PaPy_2Q)]^+$ and $[Mn^{III}(OH)(PaPy_2N)]^+$ can be understood on the basis of thermodynamic considerations, which are strongly influenced by the ability of the latter complex to form an intramolecular hydrogen bond.

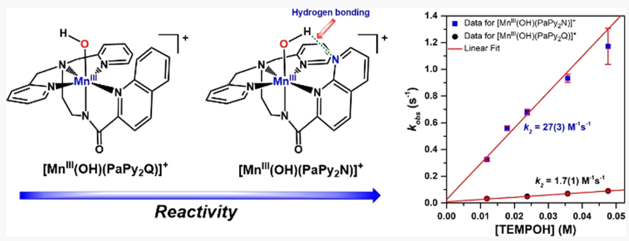

■ INTRODUCTION

Metal−oxygen adducts (i.e., metal-oxo, -peroxo, and -hydroxo species) feature prominently in the proposed mechanisms of a variety of metalloenzymes and small-molecule, synthetic catalysts.[1−7] In many cases, these metal−oxygen species are involved in critical substrate oxidation steps in the catalytic cycle. While it is now well established that high-valent metal-oxo species can be involved in such reactions, there are increasing examples of mid- and high-valent metal-hydroxo species that can effect substrate oxidation reactions.[8−17] Two metalloenzymes that rely on midvalent metal(III)-hydroxo adducts to perform their function are manganese superoxide dismutase (MnSOD) and manganese lipoxygenase (MnLOX). MnSOD regulates the levels of reactive oxygen species in the cell by catalyzing the disproportionation of superoxide to hydrogen peroxide and dioxygen.[18−20] The MnLOX enzyme catalyzes the oxidation of polyunsaturated fatty acids into their hydroperoxides, which are further metabolized into biologically active oxylipins such as a leukotrienes and jasmonates. These oxylipins act as inflammatory mediators and reproductive/growth regulators in plants.[19,21]

The MnSOD and MnLOX enzymes both feature active sites containing mononuclear Mn centers with coordinated solvent ligands (Figure 1).[19,20,22,23] When these enzymes are in their Mn^{III} oxidation states, the solvent ligand is presumed to be in the hydroxo form.[24−27] In each enzyme, the hydroxo ligand plays a critical functional role. In order to efficiently disproportionate superoxide, the $Mn^{III/II}$ reduction potential of MnSOD must lie midway between the potentials for superoxide reduction to hydrogen peroxide and oxidation to molecular oxygen (0.89 and −0.16 V vs NHE, respectively).[25,28,29] Since the $Mn^{III/II}$ reduction potential of aqueous Mn is quite high (1.51 V vs NHE), the MnSOD protein must suppress the potential by over 1 V.[30] This suppression is facilitated to a large degree by hydrogen bonding interactions between the hydroxo ligand and a glutamine residue in the second coordination sphere (Figure 1, right).[25,28,29] In MnLOX, the Mn^{III}-hydroxo unit initiates oxidation of the unsaturated fatty acid substrate by a concerted proton−electron transfer (CPET) reaction, where the Mn^{III} center

Received: June 15, 2021
Published: September 8, 2021

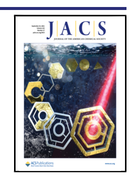

https://doi.org/10.1021/jacs.1c06199
J. Am. Chem. Soc. 2021, 143, 15159−15175

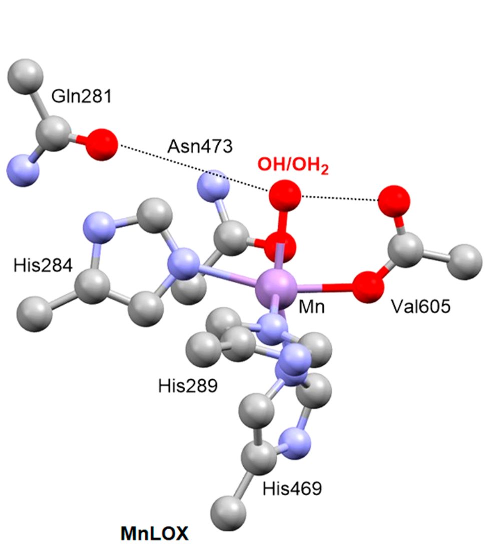

Figure 1. Active-site structures of MnLOX (left) and MnSOD (right) from PDB files 5FNO and 1VEW, respectively. Important hydrogen-bonding interactions with the coordinated solvent ligand are shown with dotted lines. The coordinated carboxylate of MnLOX is labeled according to the C-terminal amino acid from which it derives.

accepts an electron and the hydroxo ligand serves as the proton acceptor.[27] Thus, redox reactions of a Mn^{III}-hydroxo unit are critical to the function of both enzymes. (CPET is a subclass of PCET, where the proton and electron are transferred in the same kinetic step.)[19,31]

Although the active sites of MnSOD and MnLOX are distinct in several ways, in each case a coordinated carboxylate is *cis* to the solvent ligand (Figure 1).[32,33] Structures of the active site of Mn^{III}SOD from DFT computations typically show the hydroxo ligand donating a hydrogen bond to the carbonyl group of this *cis* aspartate ligand.[28,34,35] A similar hydrogen bond may be inferred for the Mn^{III}LOX active site (Figure 1, left). While there are numerous studies discussing the importance of the hydrogen bond between coordinated solvent and the second-sphere glutamine ligand in MnSOD,[20] comparatively less attention has been focused toward the consequences of the putative hydrogen bond between the hydroxo and carboxylate ligands in either MnSOD or MnLOX.

Our group has sought to understand the reactivity of Mn^{III}-hydroxo complexes using synthetic model complexes. For example, using the $[Mn^{III}(OH)(dpaq)]^+$ complex and its derivatives (see Figure 2, top), we have shown that Mn^{III}-hydroxo complexes with more electron-deficient ligands show an increased rate for CPET reactions.[36−39] These rate variations were related to the increased oxidizing power of the Mn^{III} center, as marked by a $Mn^{III/II}$ reduction potential. However, the ligand variations explored in this work have effected changes only in the primary coordination sphere. As can be inferred from the MnSOD and MnLOX active sites in Figure 1, the extensive hydrogen bonding in the extended coordination sphere must also modulate the reactivity of the Mn^{III}-hydroxo unit.

Our understanding of the roles of hydrogen bonds in stabilizing unusual ligands and in contributing to particular reactions has benefitted greatly from model complexes that mimic interactions observed in metalloenzyme active sites.[41,42] For example, Borovik and co-workers have utilized a variety of tripodal ligands with intramolecular hydrogen-bond networks to demonstrate how hydrogen bonding can modulate the properties of oxo ligands for metals in moderate (Fe^{III} and Mn^{III})[43,44] to high (Fe^{IV}, Mn^{IV}, and Mn^{V})[45−47] oxidation states. The importance of the hydrogen-bond network of these tripodal ligands on O_2 activation has also been examined.[48,49] Fout and co-workers have employed an azafulvene-amine-based tripodal ligand with a second-coordination sphere cavity that tautomerize between hydrogen-bond donating to hydrogen-bond accepting configurations.[50] Metal complexes of these ligands have been employed to stabilize oxo adducts for metals in moderate oxidation states (Fe^{III} and Mn^{III})[51,52] and to support catalysts for nitrite and perchlorate reduction.[53]

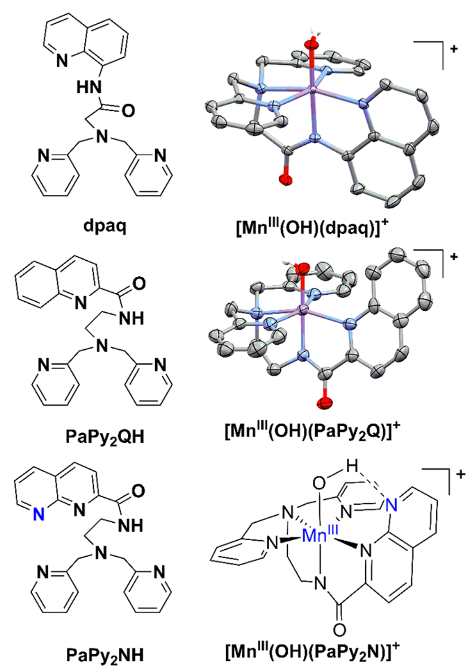

Figure 2. Structures of dpaq, $PaPy_2QH$ and $PaPy_2NH$ ligands (left) and corresponding Mn^{III}-hydroxo complexes (right). The structures for $[Mn^{III}(OH)(dpaq)]^+$ and $[Mn^{III}(OH)(PaPy_2Q)]^+$ are ORTEP renderings using the crystal structure of the triflate and perchlorate salts, respectively (see ref 39 and 40). Hydrogen atoms (except for the hydroxo proton) and counteranions were removed for clarity.

Employing a variety of ligands with hydrogen-bonding capabilities in the secondary coordination sphere, Szymczak and co-workers have explored the role of intramolecular hydrogen-bonding interactions on the properties and reactivity of late transition-metal complexes.[54−61] Additionally, Karlin et al. have reported that the introduction of an intermolecular hydrogen-bonding interaction to a synthetic, heme Fe^{IV}-oxo complex enhances the reactivity of this complex toward oxidizing C−H bonds.[62]

Of most pertinence to the MnSOD and MnLOX systems, Borovik and co-workers recently determined the influence of variations in the strength of a hydrogen-bond donor on the properties and chemical reactivity of Mn^{III}-oxo complexes.[63] These studies employed a modified tripodal ligand with a single phenylurea arm capable of donating a hydrogen bond to the oxo ligand. The strength of this hydrogen bond was modulated using phenyl substituents *para* to the HN_{urea} group. In this series, it was found that reaction rates with 9,10-dihydroanthracene (DHA) varied by more than 10-fold, with faster rates observed for complexes with electron-rich *para* substituents. On the basis of a comprehensive analysis of kinetic and thermodynamic data, it was concluded that variations in the basicity of the oxo ligand, caused by the differences in hydrogen-bond strengths, led to the observed changes in reaction rates.[63]

In the majority of these recent studies, the intramolecular hydrogen-bonding network places a hydrogen-bond donor adjacent to an oxo or hydroxo ligand. This situation is distinct from the putative hydroxo-carboxylate interaction in the Mn^{III}SOD and Mn^{III}LOX active sites, where the carboxylate acts as a hydrogen-bond acceptor for the hydroxo ligand (Figure 1). What effects does this hydrogen-bond acceptor have on the properties and reactivity of the Mn^{III}-hydroxo unit? In this present work, we address this question using a pair of Mn^{III}-hydroxo complexes, one of which contains a hydrogen-bond accepting group adjacent to the hydroxo ligand, and one of which does not. We employed the $[Mn^{III}(OH)(PaPy_2Q)]^+$ complex, previously reported by Mascharak and co-workers,[40] as the complex lacking a hydrogen bond. The crystal structure for this complex shows an aryl ring of a quinolinyl group adjacent to the hydroxo ligand (Figure 2). To introduce a hydrogen-bond acceptor, we developed a new ligand ($PaPy_2NH$), where we have substituted the quinolinyl group in $PaPy_2QH$ with a 1,8-naphthyridinyl group (Figure 2, bottom). Spectroscopic studies of $[Mn^{III}(OH)(PaPy_2Q)]^+$ and $[Mn^{III}(OH)(PaPy_2N)]^+$ confirm similar ligand binding modes in these complexes, but the consequences of the putative hydrogen-bonding interaction in the latter complex are manifested through perturbations in the electronic absorption spectrum. These conclusions are further supported by structural and spectroscopic characterization of the corresponding Mn^{III}-methoxy complexes. An assessment of the reactivities of the Mn^{III}-hydroxo complexes using a variety of substrates shows that $[Mn^{III}(OH)(PaPy_2N)]^+$ displays far more rapid rates in CPET reactions (*ca.* 15- to 100-fold rate enhancements relative to $[Mn^{III}(OH)(PaPy_2Q)]^+$). A thermodynamic analysis of the contributions to the CPET rates of these complexes provides strong support that the increased basicity of $[Mn^{III}(OH)(PaPy_2N)]^+$ leads to the enhanced reactivity of this complex. Accordingly, these studies suggest that one role of the hydroxo-carboxylate hydrogen-bonding interaction in the Mn^{III}SOD and Mn^{III}LOX systems is to enhance the oxidizing ability of the Mn^{III}-hydroxo unit by increasing the basicity of the hydroxo ligand.

■ RESULTS AND DISCUSSION

Structures and Properties of $[Mn^{II}(PaPy_2Q)](OTf)$ and $[Mn^{II}(PaPy_2N)](OTf)$ Complexes. The crystal structure of $[Mn^{II}(PaPy_2Q)](OTf)$ shows a Mn^{II} center in a distorted octahedral environment (Figure 3, left). The $PaPy_2Q$ ligand is bound in a pentadentate fashion, with *trans* pyridyl moieties and the tertiary amine and quinolinyl moieties also bound in a *trans* orientation (N4−Mn−N5 and N3−Mn−N1 angles of 145.40(9)° and 146.32(8)°, respectively; see Figure 3 for atom labels). This ligand binding mode is the same as that observed in crystal structures of corresponding Mn^{III}-hydroxo and Mn-NO complexes of the $PaPy_2Q$ ligand.[40] The Mn^{II} coordination sphere of $[Mn^{II}(PaPy_2Q)](OTf)$ is completed by an amide oxygen, derived from a separate $[Mn^{II}(PaPy_2Q)]^+$ cation, *trans* to the amide nitrogen (Figure 3, left). Similar polymeric structures have been observed for other solid-state Mn^{II} complexes supported by N_5^- ligands with carboxamido functions.[38,64]

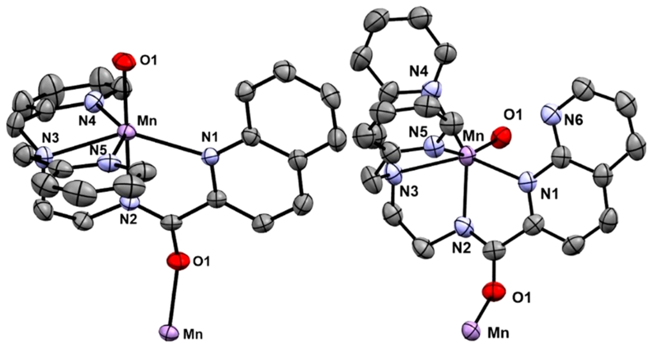

Figure 3. X-ray crystal structures of $[Mn^{II}(PaPy_2Q)](OTf)$ (left) and $[Mn^{II}(PaPy_2N)](OTf)$ (right) showing 50% probability thermal ellipsoids. The triflate counterions, solvent molecules, and hydrogen atoms were removed for clarity.

In the crystal structure of $[Mn^{II}(PaPy_2N)](OTf)$, the $PaPy_2N$ ligand is bound in a pentadentate fashion; however, in this structure the N donors from the quinolinyl, carboxamido, tertiary amine, and N4-pyridyl group are all in roughly the same plane. The amide oxygen that completes the Mn^{II} coordination sphere lies *trans* to the N5-pyridyl nitrogen. The pyridyl moieties of $[Mn^{II}(PaPy_2N)](OTf)$ are in a *cis* orientation, with a N4−Mn−N5 angle of 75.7° (Table 1), which contrasts with the *trans* orientation of the pyridines in $[Mn^{II}(PaPy_2Q)](OTf)$. Despite the different binding modes of the $PaPy_2Q$ and $PaPy_2N$ ligands, the complexes have comparable Mn^{II}-ligand bond lengths (Table 1).

The unexpected binding mode of the $PaPy_2N$ ligand might reduce steric interactions between the adjacent $[Mn^{II}(PaPy_2N)]^+$ cations in the solid state, or might reflect different crystal packing forces caused by a MeCN solvent of crystallization in the solid-state structure. To determine if a different sixth ligand would change the solid-state structure of $[Mn^{II}(PaPy_2N)](OTf)$, we attempted to grow crystals of this complex in the presence of water and with different counterions. The structure of $[Mn^{II}(PaPy_2N)](PF_6)$ is essentially identical to that of the triflate salt (see Supporting Information). Attempts to crystallize this complex in the presence of water were unsuccessful.

https://doi.org/10.1021/jacs.1c06199
J. Am. Chem. Soc. 2021, 143, 15159−15175

Table 1. Manganese-Ligand Bond Lengths (Å) and Angles (deg) from the Crystal Structures of [Mn^{II}($PaPy_2Q$)](OTf), [Mn^{II}($PaPy_2N$)](OTf), and [Mn^{II}(dpaq)](OTf)

	[Mn^{II}(L)](OTf)		
	L = $PaPy_2Q$	L = $PaPy_2N$	L = dpaq[a]
Mn−N1 (Å)	2.357(2)	2.228(3)	2.214(3)
Mn−N2 (Å)	2.148(2)	2.187(4)	2.191(3)
Mn−N3 (Å)	2.347(2)	2.344(4)	2.314(3)
Mn−N4 (Å)	2.299(2)	2.276(4)	2.244(3)
Mn−N5 (Å)	2.305(2)	2.298(4)	2.286(3)
Mn−O1 (Å)	2.0633(19)	2.119(3)	2.079(2)
O1−Mn−N2 (deg)	174.49(9)	101.06(13)	164.88(10)
N4−Mn−N5 (deg)	145.40(9)	75.68(14)	147.89(11)
N1−Mn−N3 (deg)	146.32(8)	141.70(14)	151.40(10)
N4−Mn−N2 (deg)	84.21(9)	147.36(14)	94.97(10)
N1−Mn−N2 (deg)	72.75(8)	73.95(13)	74.46(10)
N3−Mn−N2 (deg)	76.93(9)	73.52(14)	77.52(10)

[a]Data from ref.[39]

When [Mn^{II}($PaPy_2Q$)](OTf) or [Mn^{II}($PaPy_2N$)](OTf) are dissolved in MeCN, the solutions lack any defined electronic absorption bands in the visible region but show the onset of absorption intensity near 600 nm (Figure S11). These spectra are reminiscent of those of [Mn^{II}(dpaq)](OTf) and related complexes[37−39] and are consistent with the lack of any spin-allowed d−d transitions for these high-spin Mn^{II} centers. X-band EPR, ESI-MS, and solution-phase magnetic susceptibility measurements for [Mn^{II}($PaPy_2Q$)](OTf) and [Mn^{II}($PaPy_2N$)](OTf) in MeCN are consistent with mononuclear Mn^{II} centers (Figures S12−S17). Thus, the polymeric structures observed in the solid state (Figure 3) are not retained in solution. From the available spectroscopic data for the Mn^{II} complexes, we are unable to determine if the coordination mode of either the $PaPy_2Q$ or $PaPy_2N$ ligands change in solution.

Formation and Properties of Mn^{III}-hydroxo Complexes. The addition of iodosobenzene (PhIO) to either [Mn^{II}($PaPy_2Q$)](OTf) or [Mn^{II}($PaPy_2N$)](OTf) in MeCN at 25 °C results in the formation of oxidation products with electronic absorption bands in the visible region (Figure 4). For each reaction, these new chromophores are maximally formed with a minimum of 0.5 equiv of PhIO. The pink oxidation product from [Mn^{II}($PaPy_2Q$)](OTf) shows well-defined absorption bands at 485 and 734 nm (ε = 320 and 120 M^{-1} cm^{-1}, respectively). The energies and intensities of these electronic absorption bands are essentially identical to those of the Mn^{III}-hydroxo adduct [Mn^{III}(OH)($PaPy_2Q$)](ClO_4), reported by Masharak and co-workers (Figure 2).[40] ESI-MS data for the oxidized product show a prominent ion peak at an m/z value consistent with [Mn^{III}(OH)($PaPy_2Q$)]$^+$ (Figure S18). An analysis of the solution magnetic moment by the NMR method of Evans yielded μ_{eff} = 4.91 μ_B, which is close to that expected for an S = 2 system (Figure S19). In previous investigations of Mn^{III}-hydroxo complexes, we observed an equilibrium between the Mn^{III}-hydroxo complex and a μ-oxodimanganese(III,III) species.[36] One hallmark of this equilibrium was a solution magnetic moment of 0.97 μ_B, far less than that expected for a Mn^{III} center. Thus, the similarity of the solution magnetic moments of [Mn^{III}(OH)($PaPy_2Q$)]$^+$ and [Mn^{III}(OH)($PaPy_2N$)]$^+$ (*vide infra*) to the S = 2 free ion value suggest that mononuclear Mn^{III} centers are the dominant species in solution. On the basis of these data, we formulate

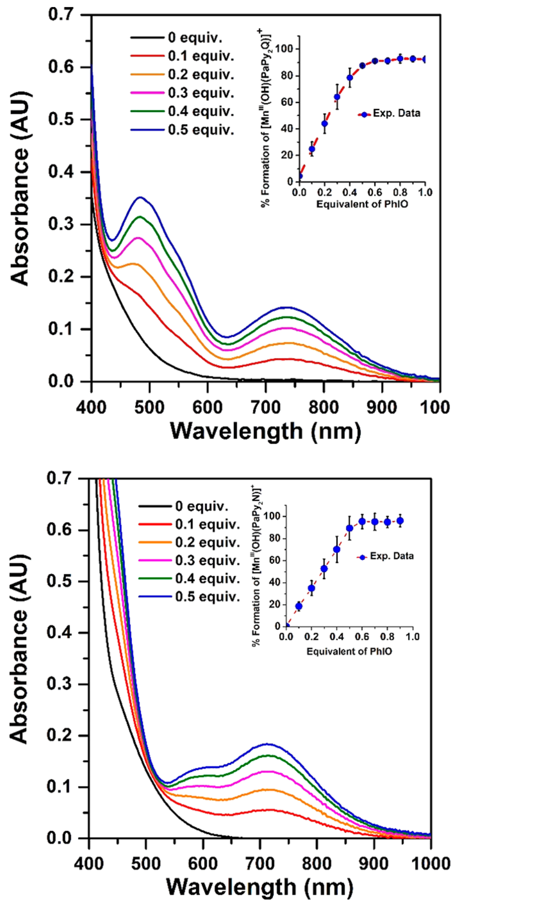

Figure 4. Electronic absorption spectroscopic titrations of [Mn^{II}($PaPy_2Q$)](OTf) (top) and [Mn^{II}($PaPy_2N$)](OTf) (bottom) with 0−1.0 equiv of PhIO in MeCN at 25 °C. The insets show the percent formation of product vs equiv added PhIO.

the product of the reaction of PhIO and [Mn^{II}($PaPy_2Q$)](OTf) in MeCN as the triflate salt of [Mn^{III}(OH)($PaPy_2Q$)]$^+$ (Figure 5). In support, treatment of [Mn^{III}(OH)($PaPy_2Q$)]$^+$ in MeCN with D_2O results in the appearance of a new peak in the ESI-MS data corresponding to the Mn^{III}−OD species (Figure S18). The reported X-ray structure of [Mn^{III}(OH)($PaPy_2Q$)](ClO_4) (Figure 2)[40] shows a structure is similar to that of [Mn^{II}($PaPy_2Q$)](OTf) (Figure 3), but with the hydroxo ligand replacing the amide oxygen.

While the reaction of PhIO with [Mn^{II}($PaPy_2Q$)](OTf) yields a pink solution, the addition of PhIO to [Mn^{II}($PaPy_2N$)](OTf) gives rise to a green solution characterized by an electronic absorption band at 730 nm (ε = 130 M^{-1} cm^{-1}) and a shoulder at 580 nm (Figure 4). The use of the NMR method of Evans to investigate this solution yields a magnetic moment (μ_{eff}) of 4.89 μ_B, supportive of the formation of a mononuclear, S = 2 Mn^{III} species (Figure S20). ESI-MS data for the green solution show a prominent ion peak at m/z of 469.12, which is as expected for the Mn^{III}-hydroxo adduct [Mn^{III}(OH)($PaPy_2N$)]$^+$ (Figure S21). The addition of D_2O to [Mn^{III}(OH)($PaPy_2N$)]$^+$ leads to a new peak with an m/z consistent with the Mn^{III}−OD analogue (Figure S21).

Our data for the PhIO oxidation products of [Mn^{II}($PaPy_2Q$)](OTf) or [Mn^{II}($PaPy_2N$)](OTf) in MeCN provide support for the formation of Mn^{III}-hydroxo complexes in each reaction. While the solution structure of [Mn^{III}(OH)($PaPy_2Q$)]$^+$ can be reasonably inferred from the crystal

https://doi.org/10.1021/jacs.1c06199
J. Am. Chem. Soc. 2021, 143, 15159−15175

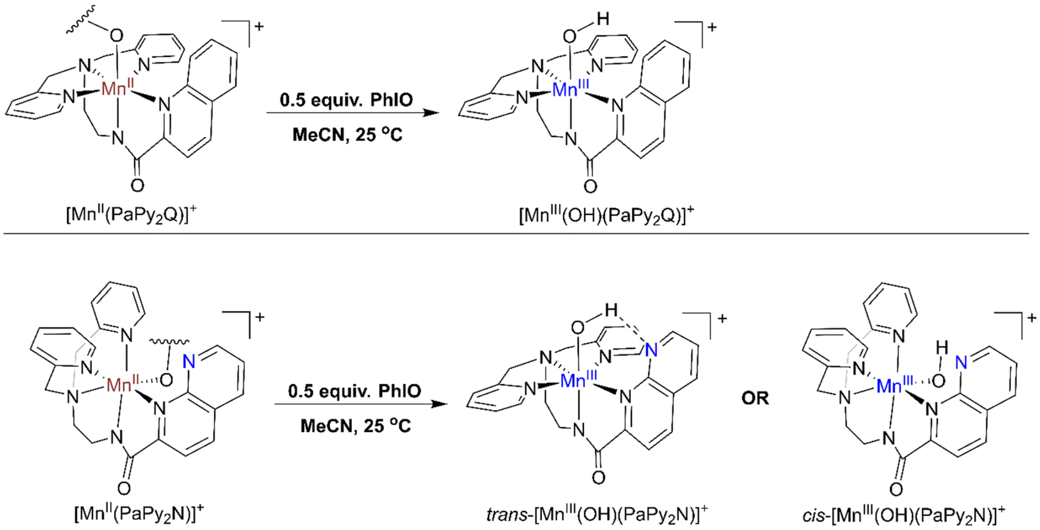

Figure 5. Schematic representation of the reactions of $[Mn^{II}(PaPy_2Q)]^+$ and $[Mn^{II}(PaPy_2N)]^+$ with PhIO to generate the Mn^{III}-hydroxo complexes $[Mn^{III}(OH)(PaPy_2Q)]^+$ and $[Mn^{III}(OH)(PaPy_2N)]^+$. Two potential structures for $[Mn^{III}(OH)(PaPy_2N)]^+$ are shown.

structure of the perchlorate salt,[40] the structure of $[Mn^{III}(OH)(PaPy_2N)]^+$ is uncertain. We propose two hypothetical structures, which we distinguish by the orientation of the pyridyl groups (*trans* or *cis*; see Figure 5, bottom-right). In *cis*-$[Mn^{III}(OH)(PaPy_2N)]^+$, the $PaPy_2N$ ligand has the same binding mode as in the corresponding Mn^{II} complex (Figure 3, right), with the hydroxo *trans* to the N5-pyridine. In *trans*-$[Mn^{III}(OH)(PaPy_2N)]^+$, the $PaPy_2N$ ligand has the same binding mode as the $PaPy_2Q$ ligand (Figure 5), with the hydroxo *trans* to the amide. In *trans*-$[Mn^{III}(OH)(PaPy_2N)]^+$, the hydroxo can serve as a hydrogen-bond donor to a nitrogen of the adjacent naphthyridinyl group.

Formation and X-ray Crystal Structures of the Mn^{III}-Methoxy Complexes $[Mn^{III}(OMe)(PaPy_2Q)](OTf)$ and $[Mn^{III}(OMe(PaPy_2N)](OTf)$. To better understand any structural differences between $[Mn^{III}(OH)(PaPy_2Q)]^+$ and $[Mn^{III}(OH)(PaPy_2N)]^+$, we generated the corresponding Mn^{III}-methoxy complexes. The reaction of 0.5 equiv. PhIO with $[Mn^{II}(PaPy_2Q)](OTf)$ or $[Mn^{II}(PaPy_2N)](OTf)$ in MeOH at 25 °C leads to the formation of chromophores with electronic absorption bands at 511 and 768 nm (ε = 480 and 120 $M^{-1}cm^{-1}$, respectively) and 485 and 768 nm (ε = 380 and 120 $M^{-1}cm^{-1}$, respectively), respectively (Figure 6). The positions and intensities of these bands are similar to those of $[Mn^{III}(OMe)(dpaq)]^+$ (λ_{max} = 510 and 760 nm, with ε = 330 and 130 M^{-1} cm^{-1}, respectively; see Table 2).[64] ESI-MS data for these complexes show peaks at m/z values consistent with the $[Mn^{III}(OMe)(PaPy_2Q)]^+$ and $[Mn^{III}(OMe)(PaPy_2N)]^+$ cations (Figures S22−S23), and magnetic moments by the NMR method of Evans are 4.87 and 4.96 μ_B, respectively (Figures S24−S25), consistent with high-spin (S = 2) Mn^{III} centers.

The oxidation products of $[Mn^{II}(PaPy_2Q)](OTf)$ and $[Mn^{II}(PaPy_2N)](OTf)$ were amenable to structural characterization by X-ray crystallography. In each case, the crystal structures are of mononuclear Mn^{III}-methoxy complexes, with the methoxy ligand bound *trans* to the carboxamido nitrogen (Figure 7). The Mn−OMe distances of 1.826(3) and 1.815(2) Å are similar to those of other Mn^{III}-methoxy complexes (Table 2).[64]

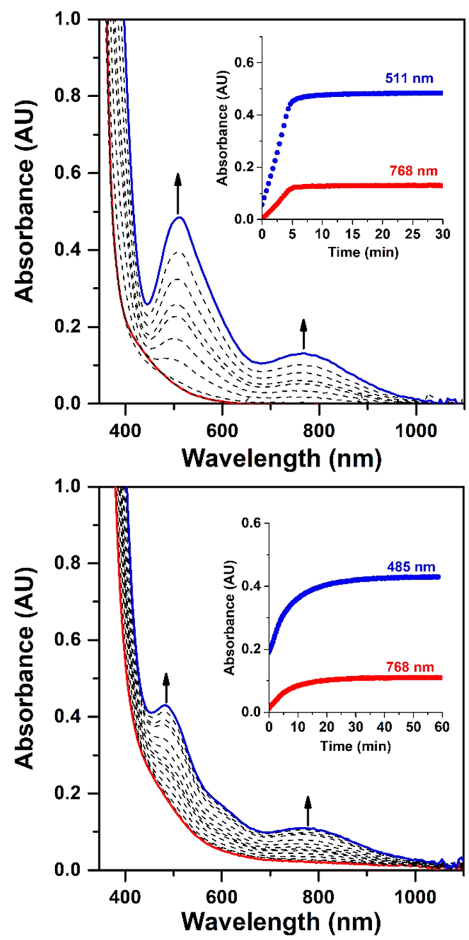

Figure 6. Electronic absorption spectra showing the reaction of 1.0 mM $[Mn^{II}(PaPy_2Q)]^+$ (top, red trace) and $[Mn^{II}(PaPy_2N)]^+$ (bottom, red trace) with 0.5 equiv of PhIO at 25 °C in MeOH. The reactions yield $[Mn^{III}(OMe)(PaPy_2Q)]^+$ (top, blue trace) and $[Mn^{III}(OMe)(PaPy_2N)]^+$ (bottom, blue trace). Inset: Time evolution of absorption signals at specified wavelengths at different time ranges.

The similar geometries of $[Mn^{III}(OMe)(PaPy_2Q)](OTf)$ and $[Mn^{III}(OMe)(PaPy_2N)](OTf)$ are in accord with their

https://doi.org/10.1021/jacs.1c06199
J. Am. Chem. Soc. 2021, 143, 15159−15175

Table 2. Manganese-Ligand Bond Lengths (Å) from the Crystal Structures of $[Mn^{III}(OMe)PaPy_2Q](OTf)$, $[Mn^{III}(OMe)(PaPy_2N)](OTf)$, $[Mn^{III}(OH)(PaPy_2Q)](ClO_4)$, and $[Mn^{III}(OMe)(dpaq)](OTf)$ and Electronic Absorption Band Maxima (nm) and Extinction Coefficients (M^{-1} cm^{-1})

	$[Mn^{III}(OMe)(L)](OTf)$			
	L = $PaPy_2Q$	L = $PaPy_2N$	L = dpaq[a]	$[Mn^{III}(OH)(PaPy_2Q)](ClO_4)$[b]
Mn−N1	2.189(3)	2.186(3)	2.051(5)	2.1945(19)
Mn−N2	1.943(3)	1.961(2)	1.979(5)	1.9680(18)
Mn−N3	2.226(3)	2.232(3)	2.175(5)	2.2415(19)
Mn−N4	2.122(3)	2.127(3)	2.203(6)	2.171(2)
Mn−N5	2.199(3)	2.184(3)	2.212(6)	2.138(2)
Mn−O2	1.826(3)	1.815(2)	1.825(4)	1.8180(16)
λ (ε)	511 (480)	485 (380)	510 (330)	485 (280)
	768 (120)	768 (120)	760 (130)	740 (120)

[a]Data from ref 64. [b]Data from ref 40.

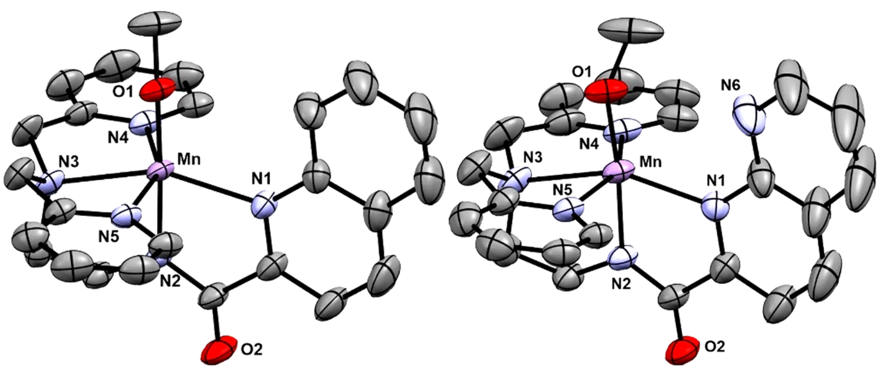

Figure 7. X-ray crystal structures of $[Mn^{III}(OMe)(PaPy_2Q)](OTf)$ (left) and $[Mn^{III}(OMe)(PaPy_2N)](OTf)$ (right) showing 50% probability thermal ellipsoid. The triflate counterions, solvent molecules, and hydrogen atoms were removed for clarity.

nearly identical electronic absorption spectra (Figure 6), which require very similar ligand-field geometries. For $[Mn^{III}(OMe)(PaPy_2Q)](OTf)$, the binding mode of the $PaPy_2Q$ ligand is the same as that observed for the Mn^{II} and Mn^{III}-hydroxo structures. The $[Mn^{III}(OMe)(PaPy_2Q)](OTf)$ and $[Mn^{III}(OH)(PaPy_2Q)](ClO_4)$ structures have nearly identical Mn^{III}−ligand bond lengths (Table 2). Surprisingly, the $PaPy_2N$ ligand in the crystal structure of $[Mn^{III}(OMe)(PaPy_2N)](OTf)$ has *trans* pyridyl groups, with the methoxy opposite the carboxamido donor. This orientation is distinct from the *cis* pyridyl geometry in the $[Mn^{II}(PaPy_2N)](OTf)$ structure (cf. Figures 7 and 3). The $PaPy_2N^-$ ligand can thus change coordination around the Mn ion in solution, suggesting that the $[Mn^{III}(OH)(PaPy_2N)](OTf)$ complex (Figure 5) could have a geometry similar to that of its Mn^{III}-methoxy analogue.

Comparison of ^1H NMR Spectra for Mn^{III}-hydroxo and Mn^{III}-methoxy Complexes. To further probe the geometries of the Mn^{III}-hydroxo and Mn^{III}-methoxy complexes, we collected room-temperature ^1H NMR data for each species. We will begin our discussion of the ^1H NMR data by focusing on $[Mn^{III}(OMe)(PaPy_2Q)](OTf)$ and $[Mn^{III}(OMe)(PaPy_2N)](OTf)$, as solid-state structures are available for each of these complexes (Figure 7). The ^1H NMR spectra of 15 mM solutions of $[Mn^{III}(OMe)(PaPy_2Q)](OTf)$ and $[Mn^{III}(OMe)(PaPy_2N)](OTf)$ in CD_3OD are very similar, each showing a set of four downfield signals from *ca.* 120 to 40 ppm, and two upfield signals near −10 and −25 ppm (Figure 8 and Table 3). The large hyperfine shifts of many of these peaks are similar to those observed for other high-spin, mononuclear Mn^{III} complexes.[65,66] The ^1H NMR spectrum of $[Mn^{III}(OMe)-$

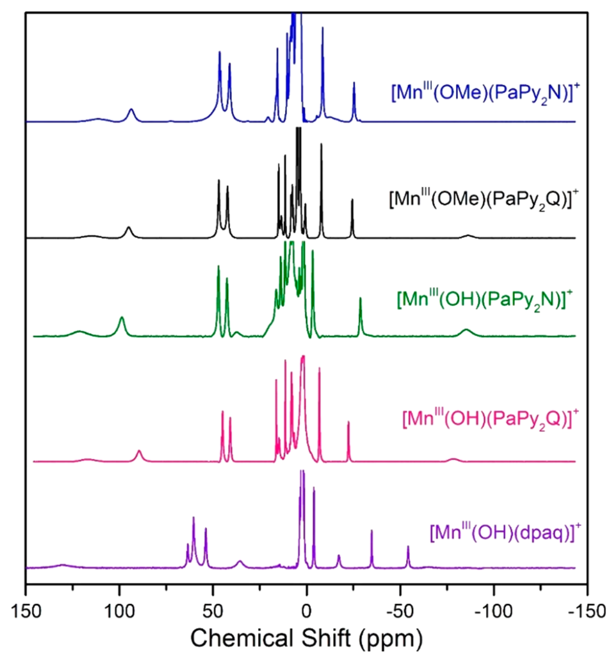

Figure 8. ^1H NMR spectra of 15 mM solutions of $[Mn^{III}(OH)(PaPy_2Q)]^+$ (pink) and $[Mn^{III}(OH)(PaPy_2N)]^+$ (green) in CD_3CN, and $[Mn^{III}(OMe)(PaPy_2Q)]^+$ (black) and $[Mn^{III}(OMe)(PaPy_2N)]^+$ (blue) in CD_3OD. All spectra are at 298 K. The spectrum of $[Mn^{III}(OH)(dpaq)]^+$ in 400 μL CD_3CN with 45 μL D_2O (purple) from ref 36 is included for comparison.

https://doi.org/10.1021/jacs.1c06199
J. Am. Chem. Soc. 2021, 143, 15159−15175

Table 3. ^{1}H NMR Chemical Shifts (ppm) for $[Mn^{III}(OMe)(L)]^+$ Complexes in CD_3OD and $Mn^{III}(OH)(L)]^+$ Complexes in CD_3CN

$[Mn^{III}(OMe)(L)]^+$			$[Mn^{III}(OH)(L)]^+$		
L = $PaPy_2Q$	L = $PaPy_2N$	L = dpaq[a]	L = $PaPy_2Q$	L = $PaPy_2N$	L = dpaq[a]
114.2	111.4	127.5 (py)	116.4	121.7	130.5 (py)
95.0	93.7	60.8 (py)	88.7	97.3	62.7 (qn)
		59.9 (qn)	44.8	47.0	60.9 (py)
		57.2 (qn)	40.8	42.4	54.3 (py)
46.9	46.4	53.9 (py)		37.4	40.5 (ND)
42.2	41.2	38.5 (CH_2)	−6.7	−3.2	−4.6 (py)
		2.54 (ND)	−22.8	−28.8	−15.5 (qn)
		−4.2 (py)	−77.0	−84.5	−33.7 (qn)
−7.9	−9.6	−15.7 (qn)			−53.8 (qn)
−24.4	−13.9	−33.6 (qn)			−63.4 (qn)
−86.2	−25.4	−52.7 (qn)			
		−66.3 (qn)			

[a]From ref 36.

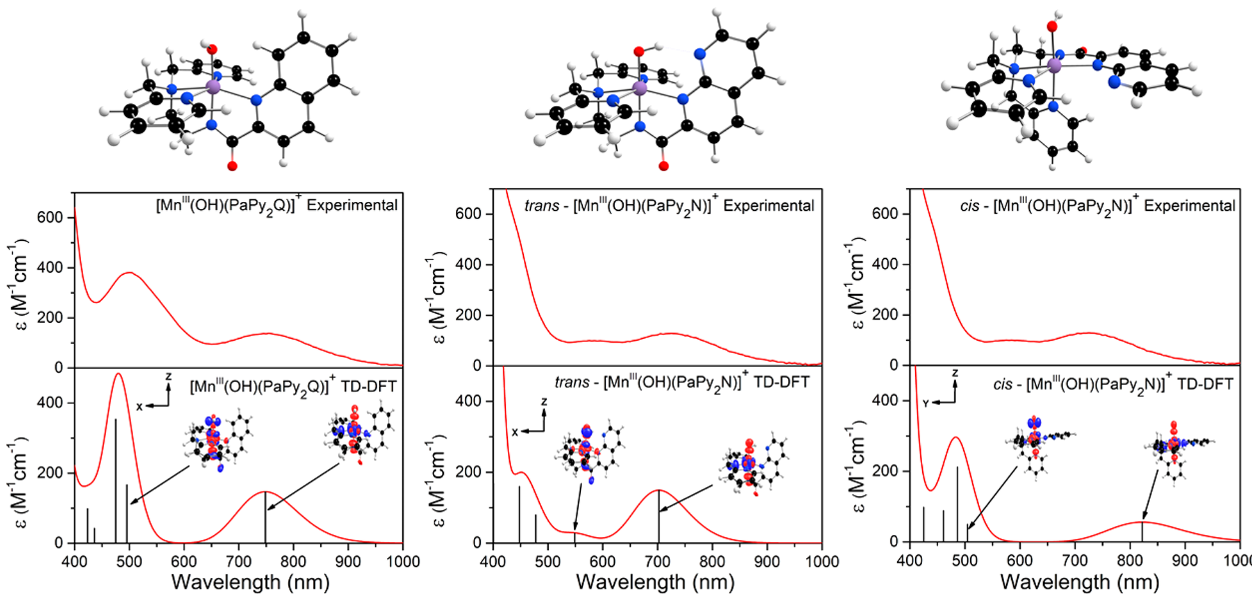

Figure 9. TD-DFT computed absorption spectra for $[Mn^{III}(OH)(PaPy_2Q)]^+$ (left), *trans*-$[Mn^{III}(OH)(PaPy_2N)]^+$ (center), and *cis*-$[Mn^{III}(OH)(PaPy_2N)]^+$ (right). The sticks indicate electronic transitions; EDDMs of selected transitions are included as an inset. Red and blue colors in the EDDMs denotes gain and loss of electron density, respectively. The DFT-computed structures of the Mn^{III}-hydoxo complexes are shown above the absorption spectra.

$(PaPy_2Q)](OTf)$ shows an additional broad resonance at −86.5 ppm that is absent in the ^{1}H NMR spectrum of $[Mn^{III}(OMe)(PaPy_2N)](OTf)$. However, the spectrum of $[Mn^{III}(OMe)(PaPy_2N)](OTf)$ contains a broad, poorly resolved peak near −14 ppm, which could correspond to the broad signal for $[Mn^{III}(OMe)(PaPy_2Q)](OTf)$ at −86.5 ppm. Overall, the pattern of hyperfine-shifted peaks for $[Mn^{III}(OMe)(PaPy_2Q)](OTf)$ and $[Mn^{III}(OMe)(PaPy_2N)]$-(OTf) are very similar, suggesting that the similarities in the solid-state structures are retained in solution.

The ^{1}H NMR spectra of the Mn^{III}-hydroxo complexes $[Mn^{III}(OH)(PaPy_2Q)](OTf)$ and $[Mn^{III}(OH)(PaPy_2N)]$-(OTf) in CD_3CN at 25 °C are nearly identical. Each spectrum shows four downfield resonances at *ca.* 120, 90, 45, and 40 ppm and three upfield peaks at *ca.* −5, −25, and −80 ppm (Figure 8). A peak-to-peak comparison of the corresponding resonances of these two complexes reveals only moderate shifts of *ca.* 2−9 ppm (Table 3). The only notable difference between the ^{1}H NMR spectra of $[Mn^{III}(OH)(PaPy_2Q)](OTf)$ and $[Mn^{III}(OH)(PaPy_2N)](OTf)$ is the low intensity peak at 37.4 ppm that is present only in the spectrum of the latter complex (Figure 8 and Table 3). In previous studies of Mn^{III}-hydroxo complexes, we have observed shifts in proton resonances caused by the addition of a small amount of water to the CD_3CN solution.[36] In this present case, the addition of 20 μL of D_2O to the 400 μL sample of $[Mn^{III}(OH)(PaPy_2Q)](OTf)$ led to the resolution of a weak peak near 52.5 ppm (Figure S26). Similarly, the addition of D_2O to $[Mn^{III}(OH)(PaPy_2N)](OTf)$ caused the disappearance of the weak signal at 37.4 ppm. Presumably, the presence of D_2O causes this peak to shift downfield such that it now overlaps with the more intense resonances near 45 ppm (Figure S26).

The ^{1}H NMR data for $[Mn^{III}(OH)(PaPy_2N)](OTf)$ allow us to reasonably infer the solution structure of this complex. If the binding mode of the $PaPy_2N$ ligand in this complex

https://doi.org/10.1021/jacs.1c06199
J. Am. Chem. Soc. 2021, 143, 15159−15175

followed that of [Mn^{II}($PaPy_2N$)](OTf), with *cis* pyridyl ligands (Figure 3), the protons of the two pyridyl groups would be inequivalent. In that case, we would expect [Mn^{III}(OH)($PaPy_2N$)](OTf) to show more resonances than [Mn^{III}(OH)($PaPy_2Q$)](OTf), [Mn^{III}(OMe)($PaPy_2Q$)](OTf), and [Mn^{III}(OMe)($PaPy_2N$)](OTf). Not only does the ^{1}H NMR spectrum of [Mn^{III}(OH)($PaPy_2N$)](OTf) lack more proton resonances than the spectra of the other complexes, the spectra of all four complexes are strikingly similar (Figure 8 and Table 3), suggesting that the ligands for these four complexes have nearly identical structures in solution. On this basis, we propose that the solution structure of [Mn^{III}(OH)($PaPy_2N$)](OTf) has the hydroxo group *trans* to the carboxamido function, with *trans* pyridyl groups (i.e., *trans*-[Mn^{III}(OH)($PaPy_2N$)]$^+$ in Figure 5).

Relative to [Mn^{III}(OH)(dpaq)]$^+$, the ^{1}H NMR spectra of [Mn^{III}(OH)($PaPy_2Q$)]$^+$ and [Mn^{III}(OH)($PaPy_2N$)]$^+$ show far fewer peaks in the upfield region. The four peaks for [Mn^{III}(OH)(dpaq)]$^+$ from −15.5 to −63.4 ppm all arise from quinolinyl protons. In addition, the 62.7 ppm resonance of [Mn^{III}(OH)(dpaq)]$^+$ was also attributed to a quinolinyl proton, and there is no corresponding peak observed for either [Mn^{III}(OH)($PaPy_2Q$)]$^+$ or [Mn^{III}(OH)($PaPy_2N$)]$^+$. Given the difference in the position of the quinolinyl (or 1,8-naphthyridinyl) moieties for these complexes, it is not unexpected that these peaks would be perturbed. Many of the quinolinyl and naphthyridinyl protons for [Mn^{III}(OH)($PaPy_2Q$)]$^+$ and [Mn^{III}(OH)($PaPy_2N$)]$^+$ are relatively far from the Mn^{III} center (the longest H···Mn separation in the X-ray structure of [Mn^{III}(OH)($PaPy_2Q$)]$^+$ is *ca.* 6.7 Å, whereas the longest distance in [Mn^{III}(OH)(dpaq)]$^+$ is 6.1 Å).[39,40] Thus, the resonances for some quinolinyl protons for [Mn^{III}(OH)($PaPy_2Q$)]$^+$ might contract toward the 10−0 ppm range. In contrast to the large perturbations in quinolinyl resonances for these complexes, the pyridyl resonances of [Mn^{III}(OH)(dpaq)]$^+$ (at 130.5, 60.9, 54.3, and −4.6 ppm) have corresponding peaks (shifted by *ca.* 10−15 ppm) in the spectra of [Mn^{III}(OH)($PaPy_2Q$)]$^+$ and [Mn^{III}(OH)($PaPy_2N$)]$^+$. A comparison of the ^{1}H NMR spectra of the Mn^{III}-methoxy complex [Mn^{III}(OMe)($PaPy_2Q$)]$^+$ and [Mn^{III}(OMe)($PaPy_2N$)]$^+$ with [Mn^{III}(OMe)(dpaq)]$^+$ also reveals minor perturbations in the positions of pyridyl protons and large changes for protons associated with the quinolinyl (or 1,8-naphthyridinyl) groups (Table 3).

Potential Structures of [Mn^{III}(OH)($PaPy_2N$)]$^+$ from DFT Computations. Due to the lack of a crystal structure for [Mn^{III}(OH)($PaPy_2N$)]$^+$, we used DFT computations to develop structures for the *trans*- and *cis*-[Mn^{III}(OH)($PaPy_2N$)]$^+$ isomers in Figure 5. The structures are shown in Figure 9 (top). A DFT-computed structure for [Mn^{III}(OH)($PaPy_2Q$)]$^+$ in the crystallographically characterized *trans* conformation gives Mn−ligand bond lengths within *ca.* 0.02 Å of the experimental distances (Table 4), supporting the use of our theoretical approach. The Mn−ligand bond lengths in *trans*-[Mn^{III}(OH)($PaPy_2N$)]$^+$ are very similar to those in the X-ray and DFT structures of [Mn^{III}(OH)($PaPy_2Q$)]$^+$ (Table 4). The Mn−N1 bond length involving the naphthyridine group is slightly shorter in *trans*-[Mn^{III}(OH)($PaPy_2N$)]$^+$ than the Mn−N1 distance in [Mn^{III}(OH)($PaPy_2Q$)]$^+$. This variation might reflect the strong hydrogen bond between the hydroxo and naphthyridine groups. This interaction is marked by a short (hydroxo)OH···N(naphthyridine) distance of 1.952 Å. The heavy atom (hydroxo)O···N(naphthyridine) separation of 2.862 Å is just slightly longer than that observed for (oxo)O···N(urea) distances in X-ray crystal structures of Mn^{III}-oxo and Mn^{III}-hydroxo adducts with intramolecular hydrogen bonds (2.613 Å).[63] Overall, the similarities between the structures of *trans*-[Mn^{III}(OH)($PaPy_2N$)]$^+$ and [Mn^{III}(OH)($PaPy_2Q$)]$^+$ are in accordance with the nearly identical ^{1}H NMR spectra of these complexes (Figure 8).

Table 4. Structural Properties for [Mn^{III}(OH)($PaPy_2Q$)]$^+$ from X-ray Crystallography and DFT Computations and Structural Properties for isomers of [Mn^{III}(OH)($PaPy_2N$)]$^+$ from DFT Computations

	[Mn^{III}(OH)($PaPy_2Q$)]$^+$		[Mn^{III}(OH)($PaPy_2N$)]$^+$	
	XRD	DFT	*trans*	*cis*
Mn−N1 (Å)	2.1945(19)	2.211	2.172	2.259
Mn−N2 (Å)	1.9680(18)	1.956	1.970	2.010
Mn−N3 (Å)	2.2415(19)	2.260	2.261	2.308
Mn−N4 (Å)	2.171(2)	2.166	2.191	2.093
Mn−N5 (Å)	2.138(2)	2.136	2.161	2.093
Mn−O2 (Å)	1.8180(16)	1.843	1.822	1.832
OH···N (Å)			1.952	
N2−Mn−O2 (deg)	174.21	176.2	176.7	173.54

In the structure of *cis*-[Mn^{III}(OH)($PaPy_2N$)]$^+$, the hydroxo group is *trans* to a pyridyl donor and *cis* to the carboxamide function, which prevents any intramolecular hydrogen bonding with the naphthyridinyl ligand (Figure 9, top-right). The Mn−N(pyridyl) (N4 and N5) distances in this structure are shorter than those of the *trans* isomer by 0.1 Å. All other Mn-ligand bond lengths are elongated in the *cis* structure.

Although TD-DFT calculations have known drawbacks, this method has performed quite well for mononuclear Mn^{III} complexes,[67−71] potentially because the electronic absorption spectra of these complexes are dominated by ligand-field transitions. In support, the TD-DFT absorption spectrum for [Mn^{III}(OH)($PaPy_2Q$)]$^+$ is in excellent agreement with experimental data, with both spectra showing features at *ca.* 750 and 500 nm (Figure 9, left). An analysis of the electron-density difference maps for the states contributing to these bands readily supports their assignments as Mn^{III} ligand-field transitions. Using a coordinate system where the *z*-axis lies along the Mn−OH bond and the *x*- and *y*-axes coincide with the equatorial Mn−ligand bonds, [Mn^{III}(OH)($PaPy_2Q$)]$^+$ has a $(d_{xy})^1(d_{yz})^1(d_{xz})^1(d_{x^2-y^2})^1(d_{z^2})^0$ ground configuration. As shown in an MO energy-level diagram in Figure S27 and MO plots in Figure S28, the highest-energy d_{z^2} MO is strongly destabilized by σ-antibonding interactions with the hydroxo and carboxamido donors, while the $d_{x^2-y^2}$ MO is σ-antibonding with respect to the equatorial ligands. The d_{xz} and d_{yz} MOs have weak π-antibonding interactions with the hydroxo ligand, and the d_{xy} MO is essentially nonbonding (Figure S28). From the TD-DFT calculations for [Mn^{III}(OH)($PaPy_2Q$)]$^+$, the lower-energy band at 750 nm is due to a one-electron $d_{x^2-y^2} \rightarrow d_{z^2}$ transition, while the higher-energy band near 500 nm contains contributions from one-electron $d_{xz} \rightarrow d_{z^2}$ and $d_{yz} \rightarrow d_{z^2}$ transitions (Figure S27). Electron-density difference maps (EDDMs) for the $d_{x^2-y^2} \rightarrow d_{z^2}$ and $d_{yz} \rightarrow d_{z^2}$ transitions are shown in Figure 9.

The TD-DFT absorption spectrum for *trans*-[Mn^{III}(OH)($PaPy_2N$)]$^+$ has bands at 700, 550, and 450 nm, which are in excellent agreement with the experimental features at 730, 580, and 450 nm (Figure 9, center). The TD-DFT calculations for

https://doi.org/10.1021/jacs.1c06199
J. Am. Chem. Soc. 2021, 143, 15159−15175

trans-$[Mn^{III}(OH)(PaPy_2N)]^+$ also reproduce the spectral changes relative to $[Mn^{III}(OH)(PaPy_2Q)]^+$. First, the TD-DFT calculations predict the lowest-energy band of *trans*-$[Mn^{III}(OH)(PaPy_2N)]^+$ (a $d_{x^2-y^2} \rightarrow d_{z^2}$ excitation) to be blue-shifted compared to that of $[Mn^{III}(OH)(PaPy_2Q)]^+$ (700 and 750 nm, respectively), which is in excellent agreement with the experimental band shift (730 and 750 nm, respectively). A comparison of MO energy-level diagrams for *trans*-$[Mn^{III}(OH)(PaPy_2N)]^+$ and $[Mn^{III}(OH)(PaPy_2Q)]^+$ reveals that this band shift arises from a modest destabilization of the d_{z^2} MO for the former complex (Figure S27), which is caused by a slight contraction in Mn−OH distance (Table 4). This contraction could arise from the hydrogen-bonding interaction that increases the basicity of the hydroxo ligand in *trans*-$[Mn^{III}(OH)(PaPy_2N)]^+$. Second, the $d_{yz} \rightarrow d_{z^2}$ transition of *trans*-$[Mn^{III}(OH)(PaPy_2N)]^+$ is red-shifted compared to that of $[Mn^{III}(OH)(PaPy_2Q)]^+$ (Figure 9). This shift accounts for the weak feature observed near 600 nm for $[Mn^{III}(OH)(PaPy_2N)]^+$ that is absent in the corresponding spectrum of $[Mn^{III}(OH)(PaPy_2Q)]^+$. The d_{yz} MO of *trans*-$[Mn^{III}(OH)(PaPy_2N)]^+$ has strong π-antibonding interactions with the hydroxo ligand (Figure S29). In contrast, the d_{xz} MO of *trans*-$[Mn^{III}(OH)(PaPy_2N)]^+$ is greatly stabilized due to the hydrogen-bonding interaction (Figure S27 and S29). This stabilization causes this transition to shift to higher energy, accounting for the low absorption intensity observed for *trans*-$[Mn^{III}(OH)(PaPy_2N)]^+$ near 475 nm. (The two remaining transitions in this region are weak charge-transfer bands.) Thus, the hydrogen bond present in *trans*-$[Mn^{III}(OH)(PaPy_2N)]^+$ causes a splitting of the d_{yz} and d_{xz} MOs (Figure S27) that leads to the corresponding $d_{yz} \rightarrow d_{z^2}$ and $d_{xz} \rightarrow d_{z^2}$ electronic transitions to shift to lower and higher energy, respectively. Accordingly, the TD-DFT absorption spectrum of *trans*-$[Mn^{III}(OH)(PaPy_2N)]^+$ reproduces all the spectral perturbations observed experimentally, and these computations allow us to link these perturbations to the hydrogen-bonding observed in this structure.

In contrast, the TD-DFT absorption spectrum for *cis*-$[Mn^{III}(OH)(PaPy_2N)]^+$ is in poorer agreement with the experimental spectrum and does not reproduce the spectral perturbations relative to $[Mn^{III}(OH)(PaPy_2Q)]^+$ (Figure 9). The lowest-energy transition for *cis*-$[Mn^{III}(OH)(PaPy_2N)]^+$ is at *ca.* 830 nm, which is significantly lower than the experimental band (720 nm). The low-energy of this transition arises from a notable contraction of the energy gap between the $d_{x^2-y^2}$ and d_{z^2} MOs for *cis*-$[Mn^{III}(OH)(PaPy_2N)]^+$ (Figure S27). In this complex, the $d_{x^2-y^2}$ MO is σ-antibonding with respect to the amide nitrogen, which causes this MO to shift to higher energy. The $d_{xz} \rightarrow d_{z^2}$ transition in *cis*-$[Mn^{III}(OH)(PaPy_2N)]^+$, observed at *ca.* 500 nm, is essentially unchanged relative to that of $[Mn^{III}(OH)(PaPy_2Q)]^+$. On the basis of these results, only the *trans*-$[Mn^{III}(OH)(PaPy_2N)]^+$ isomer can account for the spectral perturbations relative to $[Mn^{III}(OH)(PaPy_2Q)]^+$. The TD-DFT computation for the Mn^{III}-methoxy complexes was also performed, and the results nicely reproduced the experimental electronic spectra of the methoxy complexes (Figure S30).

TEMPOH Oxidation by Mn^{III}-hydroxo complexes. The reactivity of $[Mn^{III}(OH)(PaPy_2Q)]^+$ and $[Mn^{III}(OH)(PaPy_2N)]^+$ were compared using the substrate TEMPOH, which is known for its thermochemical preference to react by a CPET mechanism.[72] This preference stems from the relatively weak O−H bond dissociation free energy of TEMPOH (BDFE = 66.5 kcal mol^{-1} in MeCN at 298 K) compared to its poor acidity (pK_a = 41 in MeCN) and difficulty in oxidation ($TEMPOH^{+/\cdot}$ $E_{p,a}$ = 0.71 V vs $Fc^{+/0}$). In addition, TEMPOH has been previously employed to assess reactivity differences for Mn^{III}-hydroxo complexes and thus provides an excellent point of reference.[16,37−39,73]

The addition of excess TEMPOH to MeCN solutions of either $[Mn^{III}(OH)(PaPy_2Q)]^+$ or $[Mn^{III}(OH)(PaPy_2N)]^+$ at −35 °C led to the disappearance of the electronic absorption signals characteristic of these Mn^{III}-hydroxo adducts (Figure 10). In each case, the decay of the absorption bands could be fit to a pseudo-first-order process to at least five half-lives to give k_{obs} values. When using 10 equiv of TEMPOH relative to the Mn^{III}-hydroxo concentration, the electronic absorption signals of $[Mn^{III}(OH)(PaPy_2Q)]^+$ decayed completely over the course of *ca.* 200 s (Figure 10, top). In contrast, when the same reaction was performed with $[Mn^{III}(OH)(PaPy_2N)]^+$, the signals associated with the Mn^{III}-hydroxo adduct disappeared within *ca.* 15 s (Figure 10, center). In each case, the absorption spectra of the product solutions were consistent with the formation of the Mn^{II} starting complexes (Figure 10). X-band EPR experiments of the product solutions in perpendicular mode are dominated by signals associated with the TEMPO radical (Figures S12 and S15). Spin quantification reveals TEMPO formation of 75 ± 15% and 79 ± 15% relative to the $[Mn^{III}(OH)(PaPy_2Q)]^+$ and $[Mn^{III}(OH)(PaPy_2N)]^+$ concentrations, respectively. Collectively, these results support a reaction where the Mn^{III}-hydroxo adduct abstracts a hydrogen atom from TEMPOH to yield the corresponding Mn^{II}-aqua species and TEMPO radical.

To more thoroughly compare the rate differences for $[Mn^{III}(OH)(PaPy_2Q)]^+$ and $[Mn^{III}(OH)(PaPy_2N)]^+$, we collected k_{obs} values at different TEMPOH concentrations. For each complex, a plot of k_{obs} versus substrate concentration was linear (Figure 10, bottom), and the slope was taken as the second-order rate constant (k_2). Using this procedure, we determined k_2 values of 1.7(1) and 27(3) M^{-1} s^{-1} for TEMPOH oxidation by $[Mn^{III}(OH)(PaPy_2Q)]^+$ and $[Mn^{III}(OH)(PaPy_2N)]^+$, respectively, at −35 °C. Thus, the latter complex shows a 15-fold rate enhancement. Table 5 compares these second-order rate constants with those determined for $[Mn^{III}(OH)(dpaq)]^+$ and its derivatives. The rate constant for TEMPOH oxidation for $[Mn^{III}(OH)(PaPy_2N)]^+$ is nearly 4-fold faster than that of the previously reported $[Mn^{III}(OH)(dpaq^{5NO2})]^+$ complex (k_2 = 27(3) and 7(1) M^{-1} s^{-1}, respectively), which has the fastest TEMPOH oxidation rate of the $[Mn^{III}(OH)(dpaq^R)]^+$ series.[37] The k_2 value observed for $[Mn^{III}(OH)(PaPy_2Q)]^+$ is nearly identical to that reported for the unmodified $[Mn^{III}(OH)(dpaq)]^+$ complex (1.1(1) M^{-1} s^{-1}).[36]

Activation parameters for the reaction of TEMPOH with $[Mn^{III}(OH)(PaPy_2Q)]^+$ and $[Mn^{III}(OH)(PaPy_2N)]^+$ were obtained by collecting k_{obs} values (using 10 equiv. TEMPOH) from −35 to 15 °C for the former complex and −35 to 0 °C for the latter complex (the rate of TEMPOH oxidation by $[Mn^{III}(OH)(PaPy_2N)]^+$ was too fast at 15 °C to obtain reliable kinetic data). These data are shown in Figure 11 (top). An Eyring analysis of the variable-temperature rate data yields the free energy of activation ($\Delta G^{\ddagger}$), enthalpy of activation ($\Delta H^{\ddagger}$), and entropy of activation ($\Delta S^{\ddagger}$) values shown in Table 5 and summarized in Figure 11 (bottom). Activation parameters for Mn^{III}-hydroxo complexes in similar coordination spheres are included for comparison. For this series, the $\Delta H^{\ddagger}$ values fall

https://doi.org/10.1021/jacs.1c06199
J. Am. Chem. Soc. 2021, 143, 15159−15175

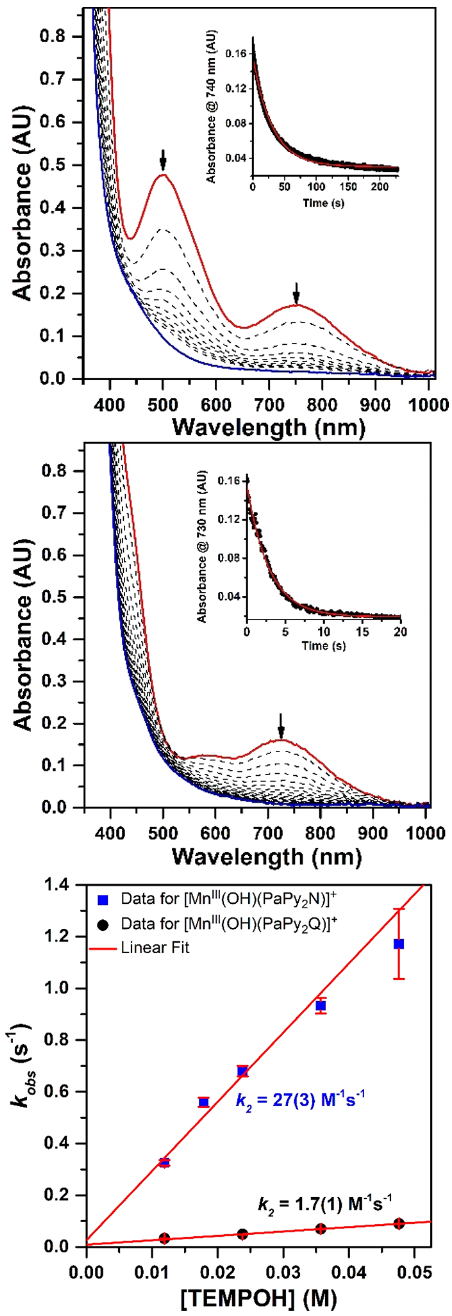

Figure 10. Reactions of 1.25 mM $[Mn^{III}(OH)(PaPy_2Q)]^+$ (top) and $[Mn^{III}(OH)(PaPy_2N)]^+$ (center) with 10 equiv of TEMPOH in MeCN at −35 °C. The inset shows the decay of the electronic absorption signal over time (black dots) and a fit (red trace) to a first-order decay. Bottom: Plot of first-order rate constants versus TEMPOH concentration. The error bars represent ± one standard deviation.

within the narrow range of 5.1−6.1 kcal mol^{-1}, with the $[Mn^{III}(OH)(PaPy_2Q)]^+$ and $[Mn^{III}(OH)(PaPy_2N)]^+$ complexes being on the higher end of this range. The $\Delta S^{\ddagger}$ values show more variation (−43 to −35 cal mol^{-1} K^{-1}), with $[Mn^{III}(OH)(PaPy_2N)]^+$ having the lowest value. It is possible that the lower entropy of activation of $[Mn^{III}(OH)(PaPy_2N)]^+$ is related to the intramolecular hydrogen bond that constrains the position of the hydroxo ligand in the reactant. In the other Mn^{III}-hydroxo complexes, the hydroxo ligands should have greater rotational degrees of freedom in the reactants that are lost in the transition state, when interactions with the substrate O−H bond constrain the position of the hydroxo ligand. While this hypothesis could be evaluated using electronic structure computations, challenges in accurately calculating entropies, coupled with the small differences in the experimental $\Delta S^{\ddagger}$ values, would make such a prediction difficult to verify. The combination of activation enthalpies and entropies for these Mn^{III}-hydroxo complexes give $\Delta G^{\ddagger}$ values from 16 to 18 kcal mol^{-1}, with the most reactive $[Mn^{III}(OH)(PaPy_2N)]^+$ having the lowest free energy of activation for the series. The small variation of activation enthalpies for the reactivity of this series of Mn^{III}-hydroxo complexes with TEMPOH is quite similar to that observed for DHA oxidation by a set of Mn^{III}-oxo complexes.[63] In that case, the $\Delta H^{\ddagger}$ values varied from 13(1) to 15(1) kcal mol^{-1}.

TEMPOH Oxidation by Mn^{III}-methoxy Complexes. Since Mn^{III}-methoxy complexes have been previously shown to be capable of effecting CPET reactions with TEMPOH,[64] we investigated the reactions of $[Mn^{III}(OMe)(PaPy_2Q)]^+$ and $[Mn^{III}(OMe)(PaPy_2N)]^+$ with TEMPOH. When either of these Mn^{III}-methoxy complexes is treated with TEMPOH in MeOH at −35 °C, the electronic absorption bands associated with the Mn^{III}-methoxy adduct undergo a rapid decay (Figure S31). Using an analysis similar to that employed for the Mn^{III}-hydroxo complexes, we determined second-order rate constants for TEMPOH oxidation by $[Mn^{III}(OMe)(PaPy_2Q)]^+$ and $[Mn^{III}(OMe)(PaPy_2N)]^+$ of 0.68(8) and 2.9(1) M^{-1} s^{-1}, respectively (Figure S31). The 4-fold rate enhancement for $[Mn^{III}(OMe)(PaPy_2N)]^+$ relative to $[Mn^{III}(OMe)(PaPy_2Q)]^+$ is far less than the 15-fold enhancement observed for the corresponding Mn^{III}-hydroxo complexes (Table 5). One cause of this difference could be that substitution of the methoxy (CH_3O^-) ligand for a hydroxo in the $PaPy_2N$-containing complexes would eliminate any potential intramolecular hydrogen-bonding interaction for the Mn^{III} complexes (hydrogen bonding would be possible for the Mn^{II}-methanol adducts formed as products of these reactions). An additional difference between the Mn^{III}-methoxy and Mn^{III}-hydroxo reactions with TEMPOH is that MeOH and MeCN were the respective solvents. This change from an aprotic to a protic solvent could have a large effect on the reaction rate. All attempts to measure TEMPOH oxidation rates for $[Mn^{III}(OMe)(PaPy_2N)]^+$ relative to $[Mn^{III}(OMe)(PaPy_2Q)]^+$ in MeCN were complicated by the reaction of the Mn^{III}-methoxy complexes with trace water to give the Mn^{III}-hydroxo species, even when using dried MeCN.

Thermodynamic Analysis of TEMPOH Oxidation Using Experimental and Computational Methods. To address the basis for the rate enhancement of $[Mn^{III}(OH)(PaPy_2N)]^+$ compared to $[Mn^{III}(OH)(PaPy_2Q)]^+$, we turned to a thermodynamic analysis of the CPET reaction.[74] CPET reactions often show a correlation between the thermodynamic driving force and the activation barrier,[75,76] as shown, for example, in our previous investigation of rate variations in TEMPOH oxidation by the series of $[Mn^{III}(OH)(dpaq^{5R})]^+$ complexes.[37] Before extending this treatment to the reaction of TEMPOH with $[Mn^{III}(OH)(PaPy_2Q)]^+$ and $[Mn^{III}(OH)(PaPy_2N)]^+$, we first discuss the thermodynamic framework for CPET reactions.

The driving force for reaction of a Mn^{III}-hydroxo adduct with TEMPOH is given by the difference in O−H BDFEs of the Mn^{II}-aqua product and the TEMPOH reactant (eq 1). For a set of reactions of different Mn^{III}-hydroxo adducts with

https://doi.org/10.1021/jacs.1c06199
J. Am. Chem. Soc. 2021, 143, 15159−15175

Table 5. Second-Order Rate Constants (k_2) and Experimental Activation Parameters for TEMPOH Oxidation by Mn^{III}-hydroxo Complexes and DFT-Calculated Thermodynamic Parameters

	Experimental				DFT-calculated		
complex	k_2 (M^{-1} s^{-1})[a]	$\Delta H^{\ddagger b}$	$\Delta S^{\ddagger c}$	$\Delta G^{\ddagger b}$	Mn^{III}/Mn^{II} $E_{1/2}$[d]	Mn^{II}–OH_2 pK_a	BDFE[b]
$[Mn^{III}(OH)(PaPy_2Q)]^+$	1.7(1)	6.1(9)	−40(4)	18(1)	−0.75	29.6	78.3
$[Mn^{III}(OH)(PaPy_2N)]^+$	27(3)	6.0(9)	−35(3)	16(1)	−1.01	38.2	84.0
$[Mn^{III}(OH)(dpaq)]^{+e}$	1.1(1)	5.3(9)	−43(4)	18(1)	−0.70	29.3	79.1
$[Mn^{III}(OH)(dpaq^{2Me})]^{+e}$	3.9(3)	5.7(3)	−41(1)	17.9(9)	−0.58	28.7	80.9
$[Mn^{III}(OH)(dpaq^{5NO2})]^{+e}$	7(1)	5.1(5)	−42(2)	18(1)	−0.51	27.8	81.2

[a]All values collected at −35 °C. [b]In kcal mol^{-1}. $\Delta G^{\ddagger}$ calculated at 25 °C. [c]In cal mol^{-1} K^{-1}. [d]In V relative to Fc^+/Fc. [e]From ref 37.

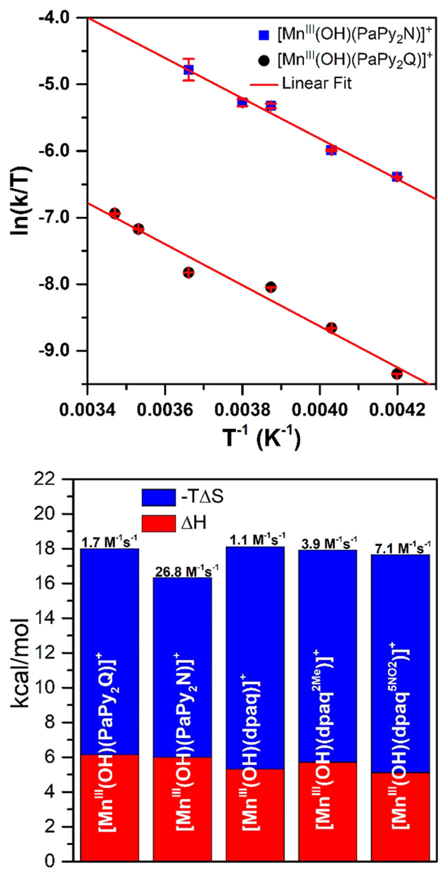

Figure 11. Top:Eyring plot of variable-temperature kinetic data for TEMPOH oxidation by $[Mn^{III}(OH)(PaPy_2Q)]^+$ and $[Mn^{III}(OH)(PaPy_2N)]^+$ in MeCN. Bottom: Bar graph showing the activation parameters and second-order rate constants for TEMPOH oxidation by various Mn^{III}-hydroxo complexes.

TEMPOH, the variation of the O–H BDFE of the Mn^{II}-aqua complex changes the reaction driving force. In this case, a stronger O–H bond in the Mn^{II}-aqua product gives faster reaction rates, with ln(k_2) linearly correlated with the Mn^{II}-aqua BDFE.[37]

$$\Delta G = \mathrm{BDFE}(\mathrm{Mn^{II}O(H)\text{–}H}) - \mathrm{BDFE}(\mathrm{TEMPO\text{–}H}) \quad (1)$$

Scheme 1 shows a square scheme where the O–H BDFE of the Mn^{II}-aqua complex is deconstructed into individual proton-transfer (vertical) and electron-transfer (horizontal) steps.[77] Using the modified Bordwell eq (eq 2),[78] the O–H BDFE can be determined from the pK_a of the Mn^{II}-aqua product, the potential of the Mn^{III}–OH/Mn^{II}–OH couple, and a constant for a given solvent and reaction conditions ($C_{G,sol}$). In our previous investigation of $[Mn^{III}(OH)(dpaq^{5R})]^+$ complexes, we observed that both the reduction potential and pK_a changed as a function of the R substitution, but changes in the potential were the larger and, therefore, dominant contribution to the change in O–H BDFE.[37]

Scheme 1. Thermodynamic Square Scheme for Decomposing the O–H BDFE of a Mn^{III}–OH/Mn^{II}–OH_2 Complex

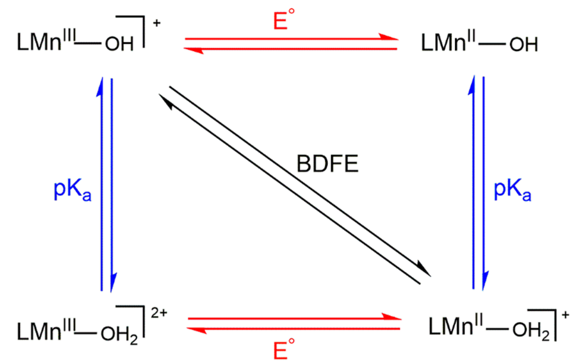

$$\mathrm{BDFE}(\mathrm{Mn^{II}O(H)\text{–}H}) = 1.37\mathrm{p}K_a + 23.06E^\circ + C_{G,sol} \quad (2)$$

On the basis of these thermodynamic considerations, the rate enhancement observed for $[Mn^{III}(OH)(PaPy_2N)]^+$ over $[Mn^{III}(OH)(PaPy_2Q)]^+$ and other Mn^{III}-hydroxo complexes very likely arises from differences in the O–H BDFEs of the Mn^{II}-aqua products. In particular, the nitrogen atom from the naphthyridinyl moiety in $[Mn^{II}(OH_2)(PaPy_2N)]^+$ could stabilize the Mn^{II}-aqua product through hydrogen bonding, whereas this type of interaction is unavailable in $[Mn^{II}(OH_2)(PaPy_2Q)]^+$. Consequently, we would expect the $[Mn^{II}(OH_2)(PaPy_2N)]^+$ product to be significantly more basic (higher pK_a) than $[Mn^{II}(OH_2)(PaPy_2Q)]^+$. It is also possible that the significant difference in the observed rate of reaction arises from differences in the $Mn^{III/II}$ reduction potentials. To evaluate these possibilities, we combined CV experiments with DFT computations.

CV experiments for $[Mn^{III}(OH)(PaPy_2Q)]^+$ and $[Mn^{III}(OH)(PaPy_2N)]^+$ in MeCN at 25 °C each reveal irreversible reduction waves with negative peak potentials ($E_{p,c}$ = −0.86 and −1.10 V vs Fc/Fc^+, respectively) (Figure S32). The peak potentials for both $[Mn^{III}(OH)(PaPy_2Q)]^+$ and $[Mn^{III}(OH)(PaPy_2N)]^+$ are more negative than those of $[Mn^{III}(OH)(dpaq)]^+$ and its derivatives ($E_{p,c}$ = −0.73 to −0.54 V).[37,39] Remarkably, $[Mn^{III}(OH)(PaPy_2N)]^+$ not only has the lowest peak potential of this series of Mn^{III}-hydroxo complexes but also shows the fastest rate of reaction for TEMPOH oxidation. Thus, these CV data reveal that $[Mn^{III}(OH)$-

https://doi.org/10.1021/jacs.1c06199
J. Am. Chem. Soc. 2021, 143, 15159–15175

$(PaPy_2N)]^+$ reacts rapidly with TEMPOH *in spite* of its very negative potential.

As we have been unable to obtain experimental insight into either the basicity of the Mn^{III}-hydroxo reactants or the acidity of the Mn^{II}-aqua products, we turned to DFT computations to obtain reasonable approximations for these parameters. We also used computations to calculate the thermodynamic $E_{1/2}$ values for the Mn^{III}−OH/Mn^{II}−OH couples, which differ slightly from the peak potentials observed by CV. The results are collected in Table 5, which also includes values for $[Mn^{III}(OH)(dpaq^R)]^+$ complexes.[37]

The calculated $E_{1/2}$ values mirror the trend in the experimental $E_{p,c}$ values, with $[Mn^{III}(OH)(PaPy_2N)]^+$ showing a more negative potential by *ca.* 250 mV (calculated $E_{1/2}$ values for $[Mn^{III}(OH)(PaPy_2Q)]^+$ and $[Mn^{III}(OH)(PaPy_2N)]^+$ are −0.75 and −1.01 V, respectively). Thus, the computations reinforce the conclusion that $[Mn^{III}(OH)(PaPy_2N)]^+$ is a significantly poorer one-electron oxidant than $[Mn^{III}(OH)(PaPy_2Q)]^+$. The p$K_a$ calculations indicate that $[Mn^{II}(OH_2)(PaPy_2N)]^+$ is considerably less acidic than $[Mn^{II}(OH_2)(PaPy_2Q)]^+$ (pK_a = 38.2 and 29.6, respectively). The basis for this large difference comes from the strong hydrogen bond in the former complex that is lacking in the latter. The DFT structures for the Mn^{II}-aqua complexes (Figure S33) reveal a short OH···N(naphthyridinyl) distance of 1.64 Å in $[Mn^{II}(OH_2)(PaPy_2N)]^+$. This interaction causes a distortion in the aqua binding position, giving an N1−Mn−O2 angle of 159°, with the aqua ligand tilted toward the naphthyridinyl group. In contrast, the corresponding angle in $[Mn^{II}(OH_2)(PaPy_2Q)]^+$, which lacks any hydrogen bond with the aqua ligand, is 170°, with the aqua angled slightly away from the quinolinyl moiety.

When combined, the calculated $E_{1/2}$ and pK_a values give O−H BDFEs for $[Mn^{II}(OH_2)(PaPy_2Q)]^+$ and $[Mn^{II}(OH_2)(PaPy_2N)]^+$ of 78.3 and 84.0 kcal mol^{-1}, respectively (Table 5 and Figure 12). The larger BDFE for $[Mn^{II}(OH_2)(PaPy_2N)]^+$ explains the higher reactivity with TEMPOH observed for the corresponding Mn^{III}-hydroxo complex. The stronger bond formed in $[Mn^{II}(OH_2)(PaPy_2N)]^+$ creates a larger driving force for the CPET reaction. The BDFE of $[Mn^{II}(OH_2)(PaPy_2Q)]^+$ is comparable to that of $[Mn^{II}(OH_2)(dpaq)]^+$ (79.1 kcal/mol), which explains their observed similar reaction rates with TEMPOH (1.7(1) and 1.1(1) M^{-1} s^{-1}, respectively; see Table 5).

When considering the reactivity of a broader series of Mn^{III}-hydroxo complexes with TEMPOH,[37] a plot of the ln(k_2) vs the O−H BDFE of Mn^{II}-aqua complexes shows a linear correlation, albeit with some scatter (Figure 12, bottom). These results reinforce the conclusion that higher O−H BDFEs in the Mn^{II}-aqua products lowers the activation barrier and increases reactivity. The $[Mn^{III}(OH)(PaPy_2N)]^+$ and $[Mn^{III}(OH)(dpaq^{OMe})]^+$ complexes provide the extremes of this series, where the *ca.* 35-fold difference in rate constants is in line with the *ca.* 5 kcal mol^{-1} difference in O−H BDFE. What is remarkable for this series is that the basis for the higher reactivities of $[Mn^{III}(OH)(PaPy_2N)]^+$ and $[Mn^{III}(OH)(dpaq^{NO2})]^+$ are of a different origin. While $[Mn^{III}(OH)(PaPy_2N)]^+$ shows a rapid reaction with TEMPOH on the basis of the basicity of this complex, it is the relatively high reduction potential of $[Mn^{III}(OH)(dpaq^{NO2})]^+$ that causes this species to be a good CPET agent. This difference is illustrated in the bar graph in Figure 12 (top), which readily displays the large contribution to the Mn^{II}-aqua BDFE from the pK_a term

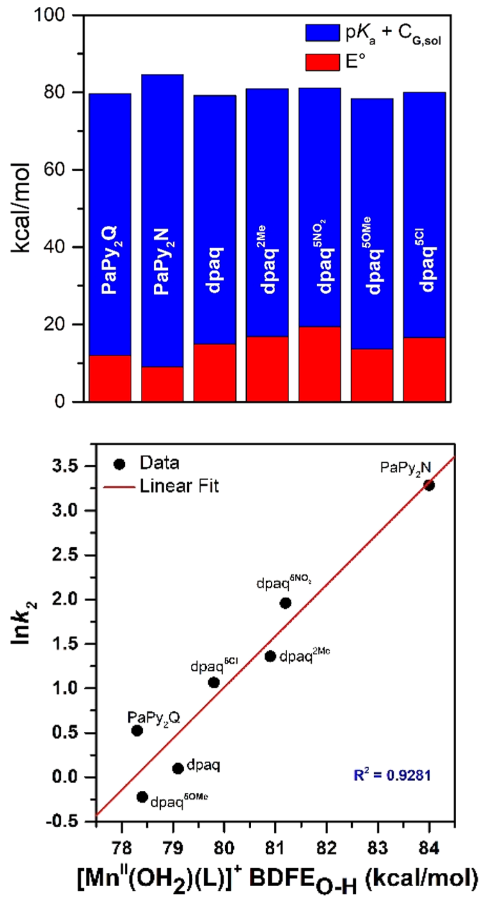

Figure 12. Top: Thermodynamic contributions to the O−H BDFE of Mn^{II}-aqua complexes from the Mn^{III}−OH/Mn^{II}−OH reduction potentials and Mn^{II}-aqua pK_a values. Bottom: Comparison of ln(k_2) for TEMPOH oxidation by Mn^{III}-hydroxo complexes as a function of the O−H BDFE of corresponding Mn^{II}-aqua complexes.

of $[Mn^{III}(OH)(PaPy_2N)]^+$ and the large contribution to the BDFE from the more positive reduction potential of $[Mn^{III}(OH)(dpaq^{NO2})]^+$.

Variation in CPET Reaction Rates of Mn^{III}-hydroxo Complexes Using Substituted Phenols. We further assessed reactivity differences between $[Mn^{III}(OH)(PaPy_2Q)]^+$ and $[Mn^{III}(OH)(PaPy_2N)]^+$ using 4-X-2,6-di-*tert*-butylphenols (4-X-2,6-DTBP), where X denotes various substituents (X = OMe, Me, ^{t}Bu, H, and Cl). By exploring reactions with these *para*-substituted phenols, we are able to correlate changes in the thermodynamic properties of the substrate with the reactivity of the Mn^{III}-hydroxo unit. In Figure 13, we show the decay of $[Mn^{III}(OH)(PaPy_2Q)]^+$ (top) and $[Mn^{III}(OH)(PaPy_2N)]^+$ (center) upon the addition of 10 equiv of 4-^{t}Bu-2,6-DTBP at 50 °C. In each case, we observe the disappearance of the electronic absorption signals associated with the Mn^{III}-hydroxo complexes and the appearance of bands at 380, 400, and 628 nm. These bands are characteristic of the 2,4,6-tri-*tert*-butylphenoxyl radical,[79] which forms as a product of this reaction in *ca.* 60% and 97% yield relative to the Mn^{III}-hydroxo concentration of $[Mn^{III}(OH)(PaPy_2Q)]^+$ and $[Mn^{III}(OH)(PaPy_2N)]^+$, respectively. X-band EPR experiments of the product solutions in perpendicular mode are dominated by signals associated with the 2,4,6-tri-*tert*-butylphenoxyl radical (Figures S12 and S15). Spin quantification reveals that this radical forms in 78 ± 15%

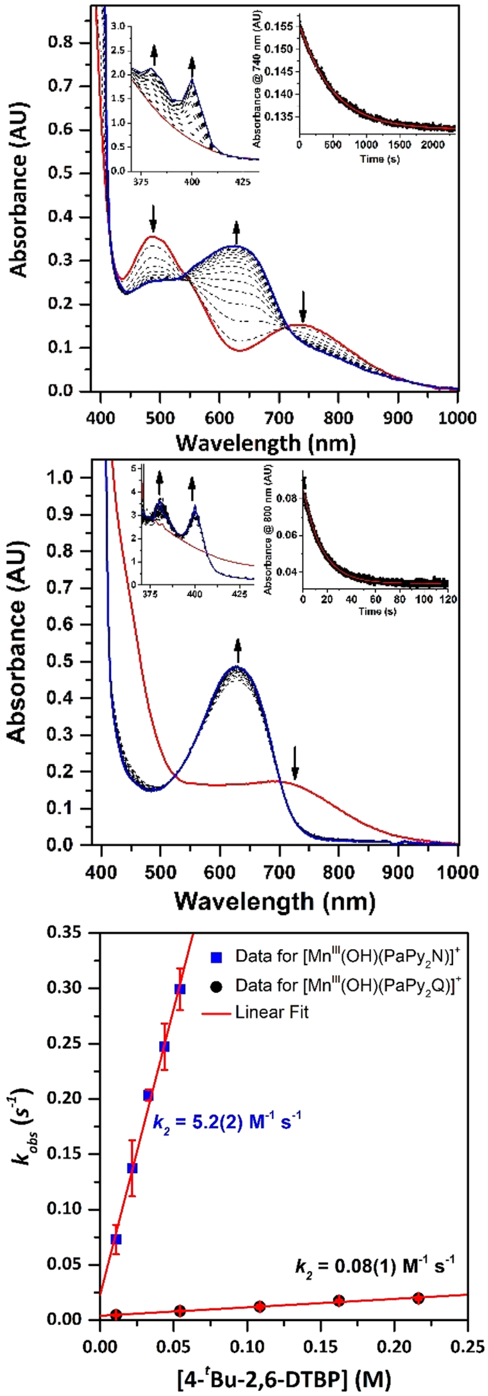

Figure 13. Reactions of 1.25 mM $[Mn^{III}(OH)(PaPy_2Q)]^+$ (top) and $[Mn^{III}(OH)(PaPy_2N)]^+$ with 10 equiv of 4-^{t}Bu-2,6-DTBP in MeCN at 50 °C (center). The inset shows the decay of the electronic absorption signal over time (black dots) and a fit (red trace) to a first-order decay. Bottom: Plot of first-order rate constants versus 4-^{t}Bu-2,6-DTBP concentration. The error bars represent ± one standard deviation.

and 91 ± 15% yield for $[Mn^{III}(OH)(PaPy_2Q)]^+$ and $[Mn^{III}(OH)(PaPy_2N)]^+$, respectively. The electronic absorption and EPR data thus indicate that both $[Mn^{III}(OH)(PaPy_2Q)]^+$ and $[Mn^{III}(OH)(PaPy_2N)]^+$ react with 4-^{t}Bu-2,6-DTBP to form the corresponding phenoxyl radical and Mn^{II} products. Reactions using different concentrations of the 4-^{t}Bu-2,6-DTBP substrate allowed us to determine k_2 values of 5.2(2) and 0.08(1) M^{-1} s^{-1} for $[Mn^{III}(OH)(PaPy_2N)]^+$ and $[Mn^{III}(OH)(PaPy_2Q)]^+$, respectively. Thus, we observe a remarkable 65-fold rate acceleration for the former complex. On the basis of our thermodynamic analysis discussed in the previous section, we infer that this rate increase comes from the enhanced thermodynamic capabilities of $[Mn^{III}(OH)(PaPy_2N)]^+$ in CPET reactions.

We performed similar experiments for the remaining 4-X-2,6-DTBP (X = OMe, Me, H, and Cl), and the data are shown in the Supporting Information (Figure S34). Second-order rate constants for each reaction are collected in (Table 6). From these data, it is immediately apparent that the k_2 for phenol oxidation by $[Mn^{III}(OH)(PaPy_2N)]^+$ is always significantly larger than that of $[Mn^{III}(OH)(PaPy_2Q)]^+$. The reactions with 4-H-2,6-DTBP provide the extreme example, where a 100-fold rate enhancement is observed. Thus, for this set of phenol substrates, $[Mn^{III}(OH)(PaPy_2N)]^+$ shows rate enhancements of 40- to 100-fold relative to $[Mn^{III}(OH)(PaPy_2Q)]^+$. We also determined activation parameters using variable-temperature kinetic experiments for the reaction of each Mn^{III}-hydroxo complex with 4-methoxy-2,6-di-*tert*-butylphenol (4-OMe-2,6-DTBP) (Figure S35 and Table S3). These experiments reveal lower $\Delta H^‡$ and $\Delta S^‡$ values for $[Mn^{III}(OH)(PaPy_2N)]^+$ compared to $[Mn^{III}(OH)(PaPy_2Q)]^+$ ($\Delta H^‡$ = 9.0(3) and 9.5(8) kcal/mol, and $\Delta S^‡$ = −34(1) and −38(3) cal mol^{-1}K^{-1}, respectively).

Table 6. Second-Order Rate Constants (k_2) for the Oxidation of 4-X-2,6-DTBP Substrates by $[Mn^{III}(OH)(PaPy_2Q)]^+$ and $[Mn^{III}(OH)(PaPy_2N)]^+$ with DFT-Computed Thermodynamic Parameters for the Phenol Substrates

	k_2 (M^{-1} s^{-1})		O−H		
substrate	$[Mn^{III}(OH)(PaPy_2Q)]^+$	$[Mn^{III}(OH)(PaPy_2N)]^+$	BDE[a]	pK_a	$E_{1/2}$[b]
4-MeO-2,6-DTBP	2.3(1)	127(2)	77.3	28.1	0.58
4-Me-2,6-DTBP	0.165(4)	8.0(4)	81.6	27.5	0.86
4-^{t}Bu-2,6-DTBP	0.08(1)	5.2(2)	82.3	28.0	0.93
4-Cl-2,6-DTBP	0.0323(1)	2.4(2)	83.5	25.4	1.17
4-H-2,6-DTBP	0.012(1)	0.99(2)	83.9	26.8	1.15

[a]In kcal mol^{-1}. [b]In V relative to Fc^+/Fc.

When the rates of 4-X-2,6-DTBP oxidation by $[Mn^{III}(OH)(PaPy_2Q)]^+$ and $[Mn^{III}(OH)(PaPy_2N)]^+$ are considered with respect to the phenol BDE, we observe a uniform decrease in the reaction rate with increasing BDE of the phenol O−H bond (Table 6). (In this analysis, we have used DFT-calculated O−H bond dissociation enthalpies, as experimental values in MeCN are not known for all the phenols considered.) A plot of ln(k_2) for phenol oxidation by both $[Mn^{III}(OH)(PaPy_2Q)]^+$ and $[Mn^{III}(OH)(PaPy_2N)]^+$ shows a linear correlation with the calculated phenol O−H bond strength (Figure 14). This behavior supports a common reaction mechanism for all phenols. The unitless slope, α, for these correlations (which was obtained by correcting the slope in the ln(k_2) versus BDE plot for thermal energy in kcal mol^{-1}; see the caption of Figure 14) is *ca.* −0.5, which is common for such linear-free energy correlations.[74] (We note that the use of the unitless slope α, rather than the slope of the plot in units of (kcal/mol)$^{-1}$, permits better comparison with values obtained from ln(k) vs ln(K_{eq}) plots.)

https://doi.org/10.1021/jacs.1c06199
J. Am. Chem. Soc. 2021, 143, 15159−15175

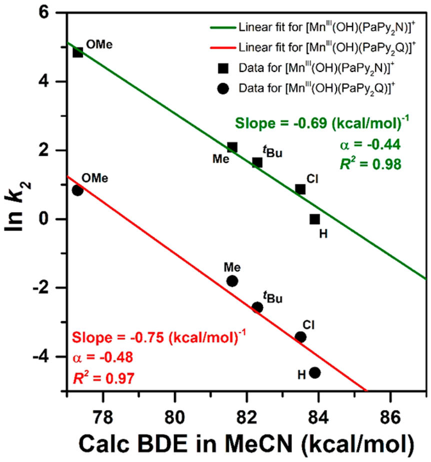

Figure 14. Plot of $\ln(k_2)$ for the oxidation of 4-X-2,6-DTBP by $[Mn^{III}(OH)(PaPy_2Q)]^+$ and $[Mn^{III}(OH)(PaPy_2N)]^+$ versus the DFT-calculated O−H BDE of the phenol substrate. The α parameter is related to the slope by the equation α = slope·RT, where R is the gas constant and T is the reaction temperature of 50 °C.

Plots of $\ln(k_2)$ versus the calculated reduction potentials ($E_{1/2}$) of the phenols are also quite linear, showing faster reaction rates for phenols with more negative potentials (Figure S36, top left). In the comparison of rate versus potential, we can determine a unitless slope of *ca.* −0.2 from plots of $(RT/F)\ \ln(k_2)$ versus $E_{1/2}$ (Figure S36, top right). This small slope indicates that the reaction rates are far less sensitive to the potential of the substrate than the O−H BDE. Tolman, Mayer, and co-workers observed similarly small slopes when investigating phenol oxidation by a pair of Cu^{III}-hydroxo complexes.[11] An analysis of the reaction rates, as $\ln(k_2)$ versus the phenol pK_a shows more significant scatter (Figure S36, bottom), although there is a general trend that more acidic phenols (i.e., 4-Cl-2,6-DTBP) show slower reaction rates. This trend tends to rule out mechanisms involving rate-limiting proton transfer, as then we would expect faster reaction rates with more acidic phenols. We therefore conclude that both $[Mn^{III}(OH)(PaPy_2Q)]^+$ and $[Mn^{III}(OH)(PaPy_2N)]^+$ perform phenol oxidation by a CPET mechanism, with rates determined by the BDE of the substrate O−H bond.

■ CONCLUSIONS

The extended coordination environments of metal catalysts play a significant role in modulating reactivity. In metalloenzymes, this extended coordination environment is created by an array of second- and third-sphere amino acid residues that work together to influence reactivity in several ways;[41] i.e., creating substrate-binding pockets, promoting coordination of exogenous ligands, or forming hydrogen bonds with first-coordination sphere amino acid residues. A prominent feature of the active sites of the MnSOD and MnLOX enzymes in the Mn^{III} state is a hydrogen bond between a coordinated hydroxo ligand and a *cis* carboxylate ligand (Figure 1).

In this present study, we have examined a pair of Mn^{III}-hydroxo complexes that differ only in one functional group of the supporting ligand. One of these complexes, $[Mn^{III}(OH)(PaPy_2N)]^+$, contains a naphthyridinyl moiety capable of forming an intramolecular hydrogen bond with the hydroxo ligand. The second complex, $[Mn^{III}(OH)(PaPy_2Q)]^+$, contains a quinolinyl moiety that does not permit any intramolecular hydrogen bonding. Using a variety of spectroscopic and computational methods, we propose that the $[Mn^{III}(OH)(PaPy_2N)]^+$ and $[Mn^{III}(OH)(PaPy_2Q)]^+$ complexes have the same coordination environments, but that the former complex contains an intramolecular hydrogen bond. In particular, the strong similarities of the ^{1}H NMR spectra of $[Mn^{III}(OH)(PaPy_2Q)]^+$ and $[Mn^{III}(OH)(PaPy_2N)]^+$ support a common ligand-binding configuration (Figure 8). In addition, computational studies of a model of $[Mn^{III}(OH)(PaPy_2N)]^+$ containing an intramolecular hydrogen bond nicely reproduce the experimental electronic absorption spectrum of this complex. Importantly, only the DFT structure for $[Mn^{III}(OH)(PaPy_2N)]^+$ with intramolecular hydrogen bonding is able to reproduce the differences in the experimental electronic absorption spectrum relative to $[Mn^{III}(OH)(PaPy_2Q)]^+$ (Figure 9).

Despite their very similar structures, $[Mn^{III}(OH)(PaPy_2N)]^+$ reacts with substrates with activated O−H bonds far more rapidly than $[Mn^{III}(OH)(PaPy_2Q)]^+$ (Figures 10 and 13). Using various substrates, we observe rate enhancements for $[Mn^{III}(OH)(PaPy_2N)]^+$ over $[Mn^{III}(OH)(PaPy_2Q)]^+$ of between 15- and 100-fold. A detailed analysis of the thermodynamic contributions to CPET reactions of $[Mn^{III}(OH)(PaPy_2Q)]^+$ and $[Mn^{III}(OH)(PaPy_2N)]^+$ reveals that the latter complex is significantly more basic. This increased basicity more than counteracts the more negative reduction potential of this complex, leading to a stronger O−H BDFE in the $[Mn^{II}(OH_2)(PaPy_2N)]^+$ product. Thus, the differences in reactivity between $[Mn^{III}(OH)(PaPy_2Q)]^+$ and $[Mn^{III}(OH)(PaPy_2N)]^+$ can be understood on the basis of thermodynamic considerations, which are strongly influenced by the ability of the latter complex to form an intramolecular hydrogen bond. Accordingly, this work suggests that the hydroxo-carboxylate hydrogen bond inferred in the active-site structures of MnSOD and MnLOX could serve a functional role by increasing the basicity of the hydroxo ligand. In the case of MnLOX, this increased basicity would activate the Mn^{III}-hydroxo unit toward CPET reactions involving the biological substrate. Of course, in our synthetic complexes, we are considering a hydrogen-bonding interaction in isolation, while enzymatic active sites contain multiple hydrogen bonds that work in concert to tune reactivity. The ability to properly reproduce the full complexity of active-site interactions in model systems remains an area of active research.

■ ASSOCIATED CONTENT

Supporting Information

The Supporting Information is available free of charge at https://pubs.acs.org/doi/10.1021/jacs.1c06199.

Materials and methods, including syntheses of ligands, metal complexes, and detailed descriptions of their characterization, X-ray data collection and crystallographic tables, TEMPOH and phenols kinetics, cyclic voltammetry, DFT calculations of thermodynamic parameters for complexes and phenol substrates, TD-DFT spectra of Mn^{III}-methoxy complexes, optimized geometry coordinates of complexes and phenol substrates. (PDF)

Accession Codes

CCDC 2046920, 2047833, 2089847, 2089852, and 2089919 contain the supplementary crystallographic data for this paper. These data can be obtained free of charge via www.ccdc.cam.ac.uk/data_request/cif, or by emailing data_request@ccdc.

https://doi.org/10.1021/jacs.1c06199
J. Am. Chem. Soc. 2021, 143, 15159−15175

cam.ac.uk, or by contacting The Cambridge Crystallographic Data Centre, 12 Union Road, Cambridge CB2 1EZ, UK; fax: +44 1223 336033.

AUTHOR INFORMATION

Corresponding Author

Timothy A. Jackson − *The University of Kansas, Department of Chemistry and Center for Environmentally Beneficial Catalysis, Lawrence, Kansas 66045, United States;* orcid.org/0000-0002-3529-2715; Phone: +(785) 864-3968; Email: taj@ku.edu

Authors

Adedamola A. Opalade − *The University of Kansas, Department of Chemistry and Center for Environmentally Beneficial Catalysis, Lawrence, Kansas 66045, United States*

Logan Hessefort − *The University of Kansas, Department of Chemistry and Center for Environmentally Beneficial Catalysis, Lawrence, Kansas 66045, United States*

Victor W. Day − *The University of Kansas, Department of Chemistry and Center for Environmentally Beneficial Catalysis, Lawrence, Kansas 66045, United States*

Complete contact information is available at: https://pubs.acs.org/10.1021/jacs.1c06199

Notes

The authors declare no competing financial interest.

ACKNOWLEDGMENTS

This work was supported by the U.S. National Science Foundation (CHE-1900384 to T.A.J. and CHE-1560279 for the summer research experience of L.H.). Support for the NMR instrumentation was provided by NIH Shared Instrumentation Grant No. S10OD016360. The U.S. NSF is also acknowledged for funds used for the purchase of X-ray instruments (CHE-0079282) and the EPR spectrometer (CHE-0946883).

REFERENCES

(1) Larson, V. A.; Battistella, B.; Ray, K.; Lehnert, N.; Nam, W. Iron and manganese oxo complexes, oxo wall and beyond. *Nature Reviews Chemistry* **2020**, *4* (8), 404−419.

(2) Rice, D. B.; Massie, A. A.; Jackson, T. A. Manganese-Oxygen Intermediates in O-O Bond Activation and Hydrogen-Atom Transfer Reactions. *Acc. Chem. Res.* **2017**, *50* (11), 2706−2717.

(3) Ray, K.; Pfaff, F. F.; Wang, B.; Nam, W. Status of reactive non-heme metal-oxygen intermediates in chemical and enzymatic reactions. *J. Am. Chem. Soc.* **2014**, *136*, 13942−13958.

(4) Puri, M.; Que, L., Jr. Toward the Synthesis of More Reactive S = 2 Non-Heme Oxoiron(IV) Complexes. *Acc. Chem. Res.* **2015**, *48*, 2443−2452.

(5) Guo, M.; Corona, T.; Ray, K.; Nam, W. Heme and Nonheme High-Valent Iron and Manganese Oxo Cores in Biological and Abiological Oxidation Reactions. *ACS Cent. Sci.* **2019**, *5* (1), 13−28.

(6) Borovik, A. S. Role of metal-oxo complexes in the cleavage of C-H bonds. *Chem. Soc. Rev.* **2011**, *40*, 1870−1874.

(7) Baglia, R. A.; Zaragoza, J. P. T.; Goldberg, D. P. Biomimetic Reactivity of Oxygen-Derived Manganese and Iron Porphyrinoid Complexes. *Chem. Rev.* **2017**, *117* (21), 13320−13352.

(8) Mandal, M.; Elwell, C. E.; Bouchey, C. J.; Zerk, T. J.; Tolman, W. B.; Cramer, C. J. Mechanisms for Hydrogen-Atom Abstraction by Mononuclear Copper(III) Cores: Hydrogen-Atom Transfer or Concerted Proton-Coupled Electron Transfer? *J. Am. Chem. Soc.* **2019**, *141* (43), 17236−17244.

(9) Pirovano, P.; McDonald, A. R. Synthetic High-Valent M-O-X Oxidants. *Eur. J. Inorg. Chem.* **2018**, *2018* (5), 547−560.

(10) Gao, H.; Groves, J. T. Fast Hydrogen Atom Abstraction by a Hydroxo Iron(III) Porphyrazine. *J. Am. Chem. Soc.* **2017**, *139* (11), 3938−3941.

(11) Dhar, D.; Yee, G. M.; Markle, T. F.; Mayer, J. M.; Tolman, W. B. Reactivity of the copper(iii)-hydroxide unit with phenols. *Chemical Science* **2017**, *8* (2), 1075−1085.

(12) Ching, W.-M.; Zhou, A.; Klein, J. E. M. N.; Fan, R.; Knizia, G.; Cramer, C. J.; Guo, Y.; Que, L. Characterization of the Fleeting Hydroxoiron(III) Complex of the Pentadentate TMC-py Ligand. *Inorg. Chem.* **2017**, *56* (18), 11129−11140.

(13) Dhar, D.; Yee, G. M.; Spaeth, A. D.; Boyce, D. W.; Zhang, H.; Dereli, B.; Cramer, C. J.; Tolman, W. B. Perturbing the Copper(III)-Hydroxide Unit through Ligand Structural Variation. *J. Am. Chem. Soc.* **2016**, *138* (1), 356−368.

(14) Kovacs, J. A. Tuning the Relative Stability and Reactivity of Manganese Dioxygen and Peroxo Intermediates via Systematic Ligand Modification. *Acc. Chem. Res.* **2015**, *48* (10), 2744−2753.

(15) Zaragoza, J. P. T.; Siegler, M. A.; Goldberg, D. P. A Reactive Manganese(IV)-Hydroxide Complex: A Missing Intermediate in Hydrogen Atom Transfer by High-Valent Metal-Oxo Porphyrinoid Compounds. *J. Am. Chem. Soc.* **2018**, *140* (12), 4380−4390.

(16) Mayfield, J. R.; Grotemeyer, E. N.; Jackson, T. A. Concerted proton-electron transfer reactions of manganese-hydroxo and manganese-oxo complexes. *Chem. Commun.* **2020**, *56* (65), 9238−9255.

(17) Jeong, D.; Yan, J. J.; Noh, H.; Hedman, B.; Hodgson, K. O.; Solomon, E. I.; Cho, J. Oxidation of Naphthalene with a Manganese(IV) Bis(hydroxo) Complex in the Presence of Acid. *Angew. Chem., Int. Ed.* **2018**, *57* (26), 7764−7768.

(18) Holley, A. K.; Bakthavatchalu, V.; Velez-Roman, J. M.; St. Clair, D. K. Manganese superoxide dismutase: guardian of the powerhouse. *Int. J. Mol. Sci.* **2011**, *12* (10), 7114−7162.

(19) Zhu, W.; Richards, N. G. J. Biological functions controlled by manganese redox changes in mononuclear Mn-dependent enzymes. *Essays Biochem.* **2017**, *61* (2), 259−270.

(20) Sheng, Y.; Abreu, I. A.; Cabelli, D. E.; Maroney, M. J.; Miller, A.-F.; Teixeira, M.; Valentine, J. S. Superoxide Dismutases and Superoxide Reductases. *Chem. Rev.* **2014**, *114* (7), 3854−3918.

(21) Chen, Y.; Wennman, A.; Karkehabadi, S.; Engström, Å.; Oliw, E. H. Crystal structure of linoleate 13R-manganese lipoxygenase in complex with an adhesion protein1. *J. Lipid Res.* **2016**, *57* (8), 1574−1588.

(22) Edwards, R. A.; Baker, H. M.; Whittaker, M. M.; Whittaker, J. W.; Jameson, G. B.; Baker, E. N. Crystal Structure of *Escherichia coli* Manganese Superoxide Dismutase at 2.1-Å Resolution. *JBIC, J. Biol. Inorg. Chem.* **1998**, *3* (2), 161−171.

(23) Wennman, A.; Oliw, E. H.; Karkehabadi, S.; Chen, Y. Crystal Structure of Manganese Lipoxygenase of the Rice Blast Fungus Magnaporthe oryzae. *J. Biol. Chem.* **2016**, *291*, 8130−8139.

(24) Miller, A.-F.; Padmakumar, F.; Sorkin, D.; Karapetian, A.; Vance, C. K. Proton-coupled Electron Transfer in Fe-superoxide Dismutase and Mn-superoxide Dismutase. *J. Inorg. Biochem.* **2003**, *93* (1−2), 71−83.

(25) Miller, A.-F. Superoxide Dismutases: Active Sites that Save, but a Protein that Kills. *Curr. Opin. Chem. Biol.* **2004**, *8*, 162−168.

(26) Su, C.; Sahlin, M.; Oliw, E. H. Kinetics of Manganese Lipoxygenase with a Catalytic Mononuclear Redox Center. *J. Biol. Chem.* **2000**, *275* (25), 18830−18835.

(27) Wennman, A.; Karkehabadi, S.; Oliw, E. H. Kinetic investigation of the rate-limiting step of manganese- and iron-lipoxygenases. *Arch. Biochem. Biophys.* **2014**, *555−556* (0), 9−15.

(28) Jackson, T. A.; Gutman, C. T.; Maliekal, J.; Miller, A.-F.; Brunold, T. C. Geometric and Electronic Structures of Manganese-Substituted Iron Superoxide Dismutase. *Inorg. Chem.* **2013**, *52* (6), 3356−3367.

(29) Vance, C. K.; Miller, A. F. Novel Insights into the Basis for *Escherichia coli* Superoxide Dismutase's Metal Ion Specificity from

Mn-Substituted FeSOD and its Very High E_m. *Biochemistry* **2001**, *40* (43), 13079−13087.
(30) Jackson, T. A.; Brunold, T. C. Combined Spectroscopic/Computational Studies on Fe- and Mn-Dependent Superoxide Dismutases: Insights into Second-Sphere Tuning of Active-Site Properties. *Acc. Chem. Res.* **2004**, *37* (7), 461−470.
(31) Azadmanesh, J.; Lutz, W. E.; Coates, L.; Weiss, K. L.; Borgstahl, G. E. O. Direct detection of coupled proton and electron transfers in human manganese superoxide dismutase. *Nat. Commun.* **2021**, *12* (1), 2079.
(32) Wennman, A.; Oliw, E. H.; Karkehabadi, S.; Chen, Y. Crystal Structure of Manganese Lipoxygenase of the Rice Blast Fungus Magnaporthe oryzae*. *J. Biol. Chem.* **2016**, *291* (15), 8130−8139.
(33) Edwards, R.; Baker, H.; Whittaker, M.; Whittaker, J. W.; Jameson, G.; Baker, E. Crystal structure of Escherichia coli manganese superoxide dismutase at 2.1-Å resolution. *JBIC, J. Biol. Inorg. Chem.* **1998**, *3*, 161−171.
(34) Jackson, T. A.; Xie, J.; Yikilmaz, E.; Miller, A.-F.; Brunold, T. C. Spectroscopic and Computational Studies on Iron and Manganese Superoxide Dismutases: Nature of the Chemical Events Associated with Active Site pKs. *J. Am. Chem. Soc.* **2002**, *124*, 10833−10845.
(35) Han, W.-G.; Lovell, T.; Noodleman, L. Coupled Redox Potentials in Manganese and Iron Superoxide Dismutases from Reaction Kinetics and Density Functional/Electrostatics Calculations. *Inorg. Chem.* **2002**, *41*, 205−218.
(36) Rice, D. B.; Jones, S. D.; Douglas, J. T.; Jackson, T. A. NMR Studies of a MnIII-hydroxo Adduct Reveal an Equilibrium between MnIII-hydroxo and μ-Oxodimanganese(III,III) Species. *Inorg. Chem.* **2018**, *57* (13), 7825−7837.
(37) Rice, D. B.; Munasinghe, A.; Grotemeyer, E. N.; Burr, A. D.; Day, V. W.; Jackson, T. A. Structure and Reactivity of (μ-Oxo)dimanganese(III,III) and Mononuclear Hydroxomanganese(III) Adducts Supported by Derivatives of an Amide-Containing Pentadentate Ligand. *Inorg. Chem.* **2019**, *58* (1), 622−636.
(38) Rice, D. B.; Wijeratne, G. B.; Burr, A. D.; Parham, J. D.; Day, V. W.; Jackson, T. A. Steric and Electronic Influence on Proton-Coupled Electron-Transfer Reactivity of a Mononuclear Mn(III)-Hydroxo Complex. *Inorg. Chem.* **2016**, *55* (16), 8110−8120.
(39) Wijeratne, G. B.; Corzine, B.; Day, V. W.; Jackson, T. A. Saturation Kinetics in Phenolic O-H Bond Oxidation by a Mononuclear Mn(III)-OH Complex Derived from Dioxygen. *Inorg. Chem.* **2014**, *53* (14), 7622−7634.
(40) Eroy-Reveles, A. A.; Leung, Y.; Beavers, C. M.; Olmstead, M. M.; Mascharak, P. K. Near-Infrared Light Activated Release of Nitric Oxide from Designed Photoactive Manganese Nitrosyls: Strategy, Design, and Potential as NO Donors. *J. Am. Chem. Soc.* **2008**, *130* (13), 4447−4458.
(41) Cook, S. A.; Hill, E. A.; Borovik, A. S. Lessons from Nature: A Bio-Inspired Approach to Molecular Design. *Biochemistry* **2015**, *54* (27), 4167−4180.
(42) Borovik, A. S. Bioinspired Hydrogen Bond Motifs in Ligand Design: The Role of Noncovalent Interactions in Metal Ion Mediated Activation of Dioxygen. *Acc. Chem. Res.* **2005**, *38* (1), 54−61.
(43) MacBeth, C. E.; Golombek, A. P.; Young, V. G.; Yang, C.; Kuczera, K.; Hendrich, M. P.; Borovik, A. S. O2 Activation by Nonheme Iron Complexes: A Monomeric Fe(III)-Oxo Complex Derived From O2. *Science* **2000**, *289* (5481), 938−941.
(44) Shirin, Z.; Hammes, B. S.; Young, V. G.; Borovik, A. S. Hydrogen Bonding in Metal Oxo Complexes: Synthesis and Structure of a Monomeric Manganese(III)-Oxo Complex and Its Hydroxo Analogue. *J. Am. Chem. Soc.* **2000**, *122* (8), 1836−1837.
(45) Parsell, T. H.; Yang, M.-Y.; Borovik, A. S. C-H Bond Cleavage with Reductants: Re-Investigating the Reactivity of Monomeric MnIII/IV-Oxo Complexes and the Role of Oxo Ligand Basicity. *J. Am. Chem. Soc.* **2009**, *131* (8), 2762−2763.
(46) Parsell, T. H.; Behan, R. K.; Green, M. T.; Hendrich, M. P.; Borovik, A. S. Preparation and Properties of a Monomeric MnIV-Oxo Complex. *J. Am. Chem. Soc.* **2006**, *128* (27), 8728−8729.
(47) Gupta, R.; Taguchi, T.; Lassalle-Kaiser, B.; Bominaar, E. L.; Yano, J.; Hendrich, M. P.; Borovik, A. S. High-spin Mn-oxo complexes and their relevance to the oxygen-evolving complex within photosystem II. *Proc. Natl. Acad. Sci. U. S. A.* **2015**, *112* (17), 5319−5324.
(48) Shook, R. L.; Borovik, A. S. Role of the Secondary Coordination Sphere in Metal-Mediated Dioxygen Activation. *Inorg. Chem.* **2010**, *49* (8), 3646−3660.
(49) Shook, R. L.; Peterson, S. M.; Greaves, J.; Moore, C.; Rheingold, A. L.; Borovik, A. S. Catalytic Reduction of Dioxygen to Water with a Monomeric Manganese Complex at Room Temperature. *J. Am. Chem. Soc.* **2011**, *133* (15), 5810−5817.
(50) Matson, E. M.; Bertke, J. A.; Fout, A. R. Isolation of Iron(II) Aqua and Hydroxyl Complexes Featuring a Tripodal H-bond Donor and Acceptor Ligand. *Inorg. Chem.* **2014**, *53* (9), 4450−4458.
(51) Gordon, Z.; Miller, T. J.; Leahy, C. A.; Matson, E. M.; Burgess, M.; Drummond, M. J.; Popescu, C. V.; Smith, C. M.; Lord, R. L.; Rodríguez-López, J.; Fout, A. R. Characterization of Terminal Iron(III)-Oxo and Iron(III)-Hydroxo Complexes Derived from O2 Activation. *Inorg. Chem.* **2019**, *58* (23), 15801−15811.
(52) Park, Y. J.; Matson, E. M.; Nilges, M. J.; Fout, A. R. Exploring Mn-O bonding in the context of an electronically flexible secondary coordination sphere: synthesis of a Mn(iii)-oxo. *Chem. Commun.* **2015**, *51* (25), 5310−5313.
(53) Ford, C. L.; Park, Y. J.; Matson, E. M.; Gordon, Z.; Fout, A. R. A bioinspired iron catalyst for nitrate and perchlorate reduction. *Science* **2016**, *354* (6313), 741−743.
(54) Wilson, J. R.; Zeller, M.; Szymczak, N. K. Hydrogen-bonded nickel(i) complexes. *Chem. Commun.* **2021**, *57* (6), 753−756.
(55) Shanahan, J. P.; Mullis, D. M.; Zeller, M.; Szymczak, N. K. Reductively Stable Hydrogen-Bonding Ligands Featuring Appended CF2-H Units. *J. Am. Chem. Soc.* **2020**, *142* (19), 8809−8817.
(56) Dahl, E. W.; Kiernicki, J. J.; Zeller, M.; Szymczak, N. K. Hydrogen Bonds Dictate O2 Capture and Release within a Zinc Tripod. *J. Am. Chem. Soc.* **2018**, *140* (32), 10075−10079.
(57) Dahl, E. W.; Dong, H. T.; Szymczak, N. K. Phenylamino derivatives of tris(2-pyridylmethyl)amine: hydrogen-bonded peroxodicopper complexes. *Chem. Commun.* **2018**, *54* (8), 892−895.
(58) Dahl, E. W.; Szymczak, N. K. Hydrogen Bonds Dictate the Coordination Geometry of Copper: Characterization of a Square-Planar Copper(I) Complex. *Angew. Chem., Int. Ed.* **2016**, *55* (9), 3101−3105.
(59) Moore, C. M.; Szymczak, N. K. Nitrite reduction by copper through ligand-mediated proton and electron transfer. *Chem. Sci.* **2015**, *6* (6), 3373−3377.
(60) Moore, C. M.; Szymczak, N. K. Redox-induced fluoride ligand dissociation stabilized by intramolecular hydrogen bonding. *Chem. Commun.* **2015**, *51* (25), 5490−5492.
(61) Moore, C. M.; Quist, D. A.; Kampf, J. W.; Szymczak, N. K. A 3-Fold-Symmetric Ligand Based on 2-Hydroxypyridine: Regulation of Ligand Binding by Hydrogen Bonding. *Inorg. Chem.* **2014**, *53* (7), 3278−3280.
(62) Ehudin, M. A.; Quist, D. A.; Karlin, K. D. Enhanced Rates of C-H Bond Cleavage by a Hydrogen-Bonded Synthetic Heme High-Valent Iron(IV) Oxo Complex. *J. Am. Chem. Soc.* **2019**, *141* (32), 12558−12569.
(63) Barman, S. K.; Jones, J. R.; Sun, C.; Hill, E. A.; Ziller, J. W.; Borovik, A. S. Regulating the Basicity of Metal-Oxido Complexes with a Single Hydrogen Bond and Its Effect on C-H Bond Cleavage. *J. Am. Chem. Soc.* **2019**, *141* (28), 11142−11150.
(64) Wijeratne, G. B.; Day, V. W.; Jackson, T. A. O-H bond oxidation by a monomeric MnIII-OMe complex. *Dalton Trans.* **2015**, *44* (7), 3295−3306.
(65) Bonadies, J. A.; Maroney, M. J.; Pecoraro, V. L. Structurally diverse manganese(III) Schiff base complexes: solution speciation via paramagnetic proton NMR spectroscopy and electrochemistry. *Inorg. Chem.* **1989**, *28* (11), 2044−2051.
(66) Ciringh, Y.; Gordon-Wylie, S. W.; Norman, R. E.; Clark, G. R.; Weintraub, S. T.; Horwitz, C. P. Multinuclear Paramagnetic NMR Spectra and Solid State X-ray Crystallographic Characterization of

Manganese(III) Schiff-Base Complexes. *Inorg. Chem.* **1997**, *36* (22), 4968−4982.
(67) Jackson, T. A.; Karapetian, A.; Miller, A.-F.; Brunold, T. C. Probing the Geometric and Electronic Structures of the Low Temperature Azide Adduct of Oxidized Manganese Superoxide Dismutase and the Product-Inhibited Complex. *Biochemistry* **2005**, *44*, 1504−1520.
(68) Jackson, T. A.; Karapetian, A.; Miller, A.-F.; Brunold, T. C. Spectroscopic and Computational Studies of the Azide-Adduct of Manganese Superoxide Dismutase: Definitive Assignment of the Ligand Responsible for the Low-Temperature Thermochromism. *J. Am. Chem. Soc.* **2004**, *126*, 12477−12491.
(69) Geiger, R. A.; Chattopadhyay, S.; Day, V. W.; Jackson, T. A. A Series of Peroxomanganese(III) Complexes Supported by Tetradentate Aminopyridyl Ligands: Detailed Spectroscopic and Computational Studies. *J. Am. Chem. Soc.* **2010**, *132* (8), 2821−2831.
(70) Colmer, H. E.; Howcroft, A. W.; Jackson, T. A. Formation, Characterization, and O-O Bond Activation of a Peroxomanganese(III) Complex Supported by a Cross-Clamped Cyclam Ligand. *Inorg. Chem.* **2016**, *55* (5), 2055−2069.
(71) Colmer, H. E.; Geiger, R. A.; Leto, D. F.; Wijeratne, G. B.; Day, V. W.; Jackson, T. A. Geometric and electronic structure of a peroxomanganese(iii) complex supported by a scorpionate ligand. *Dalton Trans.* **2014**, *43* (48), 17949−17963.
(72) Warren, J. J.; Tronic, T. A.; Mayer, J. M. Thermochemistry of Proton-Coupled Electron Transfer Reagents and its Implications. *Chem. Rev.* **2010**, *110* (12), 6961−7001.
(73) Coggins, M. K.; Brines, L. M.; Kovacs, J. A. Synthesis and Structural Characterization of a Series of MnIIIOR Complexes, Including a Water-Soluble MnIIIOH That Promotes Aerobic Hydrogen-Atom Transfer. *Inorg. Chem.* **2013**, *52* (21), 12383−12393.
(74) The thermodynamic values obtained from this analysis support our assumption that the oxidation of TEMPOH by these Mn^{III}-hydroxo complexes proceeds by a CPET mechanism rather than a stepwise process. We discuss these results in the section "DFT Calculations for Thermodynamic Parameters" in the Supporting Information.
(75) Mayer, J. M. Understanding Hydrogen Atom Transfer: From Bond Strengths to Marcus Theory. *Acc. Chem. Res.* **2011**, *44*, 36−46.
(76) Darcy, J. W.; Koronkiewicz, B.; Parada, G. A.; Mayer, J. M. A Continuum of Proton-Coupled Electron Transfer Reactivity. *Acc. Chem. Res.* **2018**, *51* (10), 2391−2399.
(77) Tyburski, R.; Liu, T.; Glover, S. D.; Hammarström, L. Proton-Coupled Electron Transfer Guidelines, Fair and Square. *J. Am. Chem. Soc.* **2021**, *143* (2), 560−576.
(78) Bordwell, F. G.; Cheng, J.; Ji, G. Z.; Satish, A. V.; Zhang, X. Bond dissociation energies in DMSO related to the gas phase values. *J. Am. Chem. Soc.* **1991**, *113* (26), 9790−9795.
(79) Manner, V. W.; Markle, T. F.; Freudenthal, J. H.; Roth, J. P.; Mayer, J. M. The first crystal structure of a monomeric phenoxyl radical: 2,4,6-tri-tert-butylphenoxyl radical. *Chem. Commun.* **2008**, No. 2, 256−258.

https://doi.org/10.1021/jacs.1c06199
J. Am. Chem. Soc. 2021, 143, 15159−15175